University of Groningen

A20 deficiency in myeloid cells protects mice from diet-induced obesity and insulin resistance due to increased fatty acid metabolism

Catrysse, Leen; Maes, Bastiaan; Mehrotra, Parul; Martens, Arne; Hoste, Esther; Martens, Liesbet; Maueröder, Christian; Remmerie, Anneleen; Bujko, Anna; Slowicka, Karolina

IMPORTANT NOTE: You are advised to consult the publisher's version (publisher's PDF) if you wish to cite from it. Please check the document version below.

Document Version
Publisher's PDF, also known as Version of record

Link to publication in University of Groningen/UMCG research database

Cell Reports

A20 deficiency in myeloid cells protects mice from diet-induced obesity and insulin resistance due to increased fatty acid metabolism

Graphical abstract

Highlights

- Myeloid A20 deficiency creates a pro-inflammatory environment in metabolic tissues

- Myeloid A20 deficiency protects mice from diet-induced obesity and insulin resistance

- Myeloid A20 deficiency promotes the expansion of inflammatory CD206+ ATMs

- A20-deficient macrophages metabolize more palmitate *in vitro* and *in vivo*
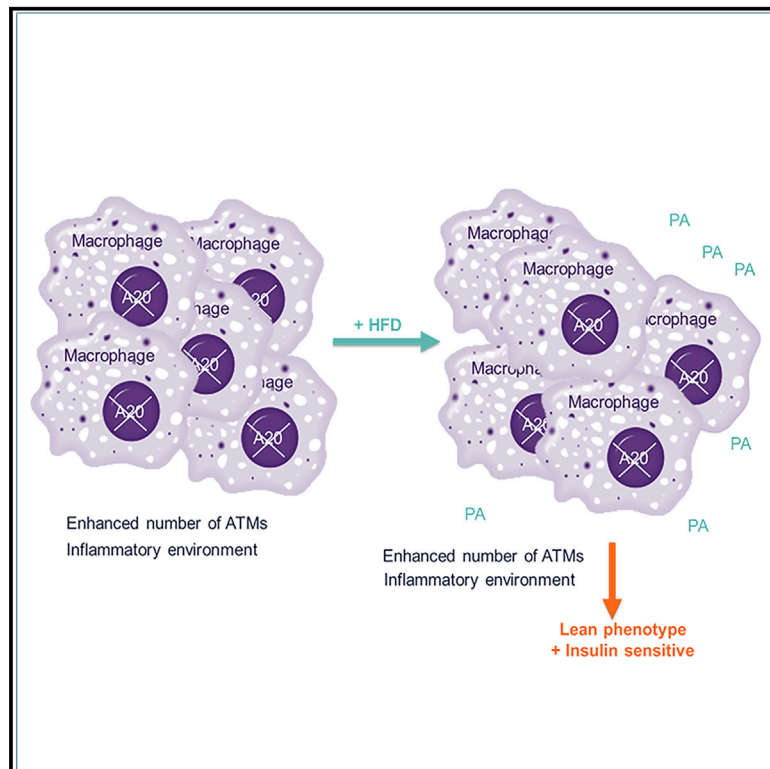
Authors

Leen Catrysse, Bastiaan Maes,
Parul Mehrotra, ..., Kodi Ravichandran,
Sophie Janssens, Geert van Loo

Correspondence

geert.vanloo@irc.vib-ugent.be

In brief

Catrysse et al. show that absence of A20 in myeloid cells leads to protection against diet-induced obesity and insulin resistance. They speculate that this is caused by increased oxygen consumption and increased fatty acid metabolism of A20-deficient macrophages. These findings reveal a role for A20 in regulating macrophage immunometabolism.

CellPress

Cell Reports

Article

A20 deficiency in myeloid cells protects mice from diet-induced obesity and insulin resistance due to increased fatty acid metabolism

Leen Catrysse,[1,2,8] Bastiaan Maes,[1,3,8] Parul Mehrotra,[1,2] Arne Martens,[1,2] Esther Hoste,[1,2] Liesbet Martens,[1,2] Christian Maueröder,[1,2] Anneleen Remmerie,[1,2] Anna Bujko,[1,2] Karolina Slowicka,[1,2] Mozes Sze,[1,2] Hanna Vikkula,[1,2] Bart Ghesquière,[4] Charlotte L. Scott,[1,2] Yvan Saeys,[1,5] Bart van de Sluis,[6] Kodi Ravichandran,[1,2,7] Sophie Janssens,[1,3] and Geert van Loo[1,2,8,9,10,*]

[1]VIB Center for Inflammation Research, B-9052 Ghent, Belgium
[2]Department of Biomedical Molecular Biology, Ghent University, 9052 Ghent, Belgium
[3]Department of Internal Medicine and Pediatrics, Ghent University, B-9052 Ghent, Belgium
[4]Metabolomics Core Facility, VIB Center for Cancer Biology, VIB, B-3000 Leuven, Belgium
[5]Department of Applied Mathematics, Computer Science and Statistics, Ghent University, B-9052 Ghent, Belgium
[6]Department of Pediatrics, Molecular Genetics Section, University of Groningen, University Medical Center Groningen, NL- 9713 Groningen, the Netherlands
[7]Center for Cell Clearance and Department of Microbiology, Immunology and Cancer Biology, University of Virginia, Charlottesville, VA, USA
[8]These authors contributed equally
[9]Senior author
[10]Lead contact
*Correspondence: geert.vanloo@irc.vib-ugent.be
https://doi.org/10.1016/j.celrep.2021.109748

SUMMARY

Obesity-induced inflammation is a major driving force in the development of insulin resistance, type 2 diabetes (T2D), and related metabolic disorders. During obesity, macrophages accumulate in the visceral adipose tissue, creating a low-grade inflammatory environment. Nuclear factor κB (NF-κB) signaling is a central coordinator of inflammatory responses and is tightly regulated by the anti-inflammatory protein A20. Here, we find that myeloid-specific A20-deficient mice are protected from diet-induced obesity and insulin resistance despite an inflammatory environment in their metabolic tissues. Macrophages lacking A20 show impaired mitochondrial respiratory function and metabolize more palmitate both *in vitro* and *in vivo*. We hypothesize that A20-deficient macrophages rely more on palmitate oxidation and metabolize the fat present in the diet, resulting in a lean phenotype and protection from metabolic disease. These findings reveal a role for A20 in regulating macrophage immunometabolism.

INTRODUCTION

The prevalence of obesity is steadily rising and has more than doubled since 1980. Obesity is closely associated with multiple metabolic disorders including insulin resistance and type 2 diabetes (T2D), non-alcoholic fatty liver disease, cardiovascular disease, and obesity-related cancers. Research over the past decade has established that obesity causes a condition of chronic low-grade inflammation, which is considered to lie at the origin of metabolic disease development (Gregor and Hotamisligil, 2011; Odegaard and Chawla, 2013). Macrophages play a central role in obesity-associated inflammation, and a lot of research has focused on the involvement of adipose tissue macrophages (ATMs) in this process (Catrysse and van Loo, 2018; Reilly and Saltiel, 2017). In steady state, the adipose tissue contains mainly tissue-resident CD206^{+} ATMs that have anti-inflammatory activity, promote tissue repair, and are important in maintaining adipose tissue homeostasis. In obese conditions,

however, the adipose tissue becomes infiltrated with large numbers of CD11c^{+} macrophages that adopt a pro-inflammatory phenotype, leading to the secretion of pro-inflammatory cytokines including tumor necrosis factor (TNF) and interleukin (IL)-1β (Osborn and Olefsky, 2012). This phenotypic switch in macrophage activity is believed to be a main driving force in the development of the low-grade inflammatory state associated with obesity.

Of particular importance in establishing this inflammatory condition is the nuclear factor κB (NF-κB) signaling pathway, which becomes activated in several metabolic tissues during obesity (Catrysse and van Loo, 2017; Könner and Brüning, 2011; Tanti et al., 2013). Previous studies have shown that inhibition of NF-κB signaling in myeloid cells protects against diet-induced systemic insulin resistance (Arkan et al., 2005). A crucial regulator of NF-κB activation is the anti-inflammatory protein A20 (also known as TNFAIP3 [tumor necrosis factor alpha induced protein 3]), which also has strong anti-apoptotic activities in many cell

types (Catrysse et al., 2014; Martens and van Loo, 2020). Interestingly, small nucleotide polymorphisms (SNPs) in or near the *A20* locus have been identified in patients suffering from several autoimmune and inflammatory diseases, including atherosclerosis and T2D (Vereecke et al., 2011). In myeloid cells, A20 is essential in controlling inflammatory responses, hence, macrophages lacking A20 show an exacerbated NF-κB response leading to the increased production of pro-inflammatory cytokines (Matmati et al., 2011). As a result, myeloid-specific A20 knockout (A20$^{myel-KO}$) mice develop a spontaneous erosive polyarthritis, a phenotype that is dependent on macrophage necroptosis and NLRP3 inflammasome activation (Matmati et al., 2011; Polykratis et al., 2019; Vande Walle et al., 2014; De Wilde et al., 2016).

Given the exacerbated inflammatory response of A20-deficient macrophages and the importance of pro-inflammatory CD11c$^+$ macrophages in the pathophysiology of obesity, here we investigated the role of A20$^{myel-KO}$ mice in the context of obesity. Although A20$^{myel-KO}$ mice develop systemic inflammation with increased macrophage numbers when fed with a high-fat diet (HFD), they are completely protected from obesity and obesity-induced insulin resistance. CD206$^+$ macrophages are shown to accumulate in the A20$^{myel-KO}$ adipose tissue after the HFD, although they have a gene signature indicative of classical pro-inflammatory macrophage activation. A20-deficient macrophages show impaired mitochondrial respiratory function and do not rely on intrinsic free fatty acid (FFA) oxidation, suggesting that they preferentially metabolize dietary fatty acids, resulting in the lean phenotype. Together, these findings reveal an unexpected role for A20 in regulating macrophage immunometabolism.

RESULTS

Myeloid A20 deficiency in mice creates a pro-inflammatory environment in metabolic tissues

A20$^{myel-KO}$ mice develop a systemic inflammatory pathology caused by hyperactive macrophages that uncontrollably produce inflammatory cytokines due to a prolonged NF-κB response (Matmati et al., 2011; Vande Walle et al., 2014). To investigate the consequence of these hyperactive macrophages in conditions of obesity, A20$^{myel-KO}$ mice and Cre-negative A20 "floxed" control littermates were subjected to either a HFD (60% kcal fat) or a standard diet (SD; 10% kcal fat) for 12 weeks. HFD-induced obesity is characterized by a condition of chronic low-grade inflammation, evidenced by the moderate increase in levels of inflammatory cytokines in the serum but also in metabolic tissues such as the adipose tissue (Osborn and Olefsky, 2012). As previously shown (Matmati et al., 2011), A20$^{myel-KO}$ mice already show high serum levels of inflammatory cytokines in unchallenged conditions compared to wild-type control mice, and these levels remain high after the HFD (Figure 1A). In addition, the splenomegaly observed in A20$^{myel-KO}$ mice is maintained in the presence of the HFD (Figure 1B). Pro-inflammatory cytokines are also upregulated in the visceral epididymal white adipose tissue (eWAT) of A20$^{myel-KO}$ mice (Figure 1C). In addition, the adipose tissue of A20$^{myel-KO}$ mice shows elevated macrophage and monocyte numbers, comparable to that seen in obese control littermates (Figure 1D). Interestingly, the typical

crown-like structures (CLSs), formed by infiltrating macrophages accumulating around dead adipocytes and evident in the eWAT from wild-type HFD mice, are completely absent in the eWAT from A20$^{myel-KO}$ mice, even when fed with the HFD (Figure 1E). Also, in the liver, A20$^{myel-KO}$ mice display elevated expression levels of pro-inflammatory cytokines (Figure 1F), increased macrophage and monocyte numbers (Figure 1G), and the presence of inflammatory foci, which are absent in control wild-type mice (Figure 1H). Together, these data demonstrate that the metabolic tissues of A20$^{myel-KO}$ mice are inflamed, which does not change in conditions of the HFD. However, typical hallmarks of obesity-associated inflammation such as the presence of CLSs are absent in A20$^{myel-KO}$ mice fed with the HFD.

Myeloid A20 deficiency protects mice from diet-induced obesity

Surprisingly, A20$^{myel-KO}$ mice are completely protected from obesity and display a similar weight curve as mice fed on the SD, in contrast to wild-type control mice that gain weight and develop obesity upon HFD feeding (Figure 2A). In agreement, A20$^{myel-KO}$ mice show reduced adiposity, as the size of both eWAT and inguinal WAT (iWAT) (Figure 2B), as well as the fat mass (Figure 2C) are strongly reduced compared to control mice on the HFD. In addition, the adipocytes in A20$^{myel-KO}$ eWAT are smaller in size, but not reduced in number (Figure 1E; Figure S1A). Liver weight and liver triglycerides levels are not increased in A20$^{myel-KO}$ mice fed with the HFD, indicating that the lipids are not being stored in the liver (Figure S1B). Notably, the lean mass of A20$^{myel-KO}$ mice fed a HFD is even increased compared with control HFD mice, indicating that A20$^{myel-KO}$ mice are overall healthy and do not lose muscle mass (Figure 2C).

Interestingly, when fed with the SD, A20$^{myel-KO}$ mice show diminished body weight gain and epididymal fat pad size compared to control mice (Figures 2A and 2B), indicating that the lean phenotype of A20$^{myel-KO}$ mice is already present at steady state. The protection against HFD-induced obesity in A20$^{myel-KO}$ mice is further confirmed by a reduced hyperlipidemia, as measured by lower levels of cholesterol, triglycerides, and FFAs in the serum of A20$^{myel-KO}$ mice compared to control mice (Figure 2D). Transfer of A20-deficient bone marrow into wild-type donor mice is sufficient to protect against diet-induced obesity, while the transfer of wild-type bone marrow into lethally irradiated A20$^{myel-KO}$ mice is enough to revert the lean phenotype into an obesity phenotype (Figure 2E). This indicates that A20 deficiency in the myeloid cells is sufficient to induce protection against diet-induced obesity. Next, to investigate if induced deletion of A20 could revert obesity in already obese mice, we generated a tamoxifen-inducible A20 knockout mouse line by using the Cx3Cr1-ERT2-targeting strategy (A20$^{Cx3Cr1-KO}$ mice) and initiated A20 deletion after 10 weeks of HFD feeding. Indeed, tamoxifen-induced A20 deletion suppresses weight gain in these mice (Figure 2F). Interestingly, when the tamoxifen treatment was stopped, A20$^{Cx3Cr1-KO}$ mice regained weight to the same extent as their wild-type littermates (Figure 2F).

ATMs play crucial roles in obesity-associated inflammation (Catrysse and van Loo, 2018; Reilly and Saltiel, 2017). To address
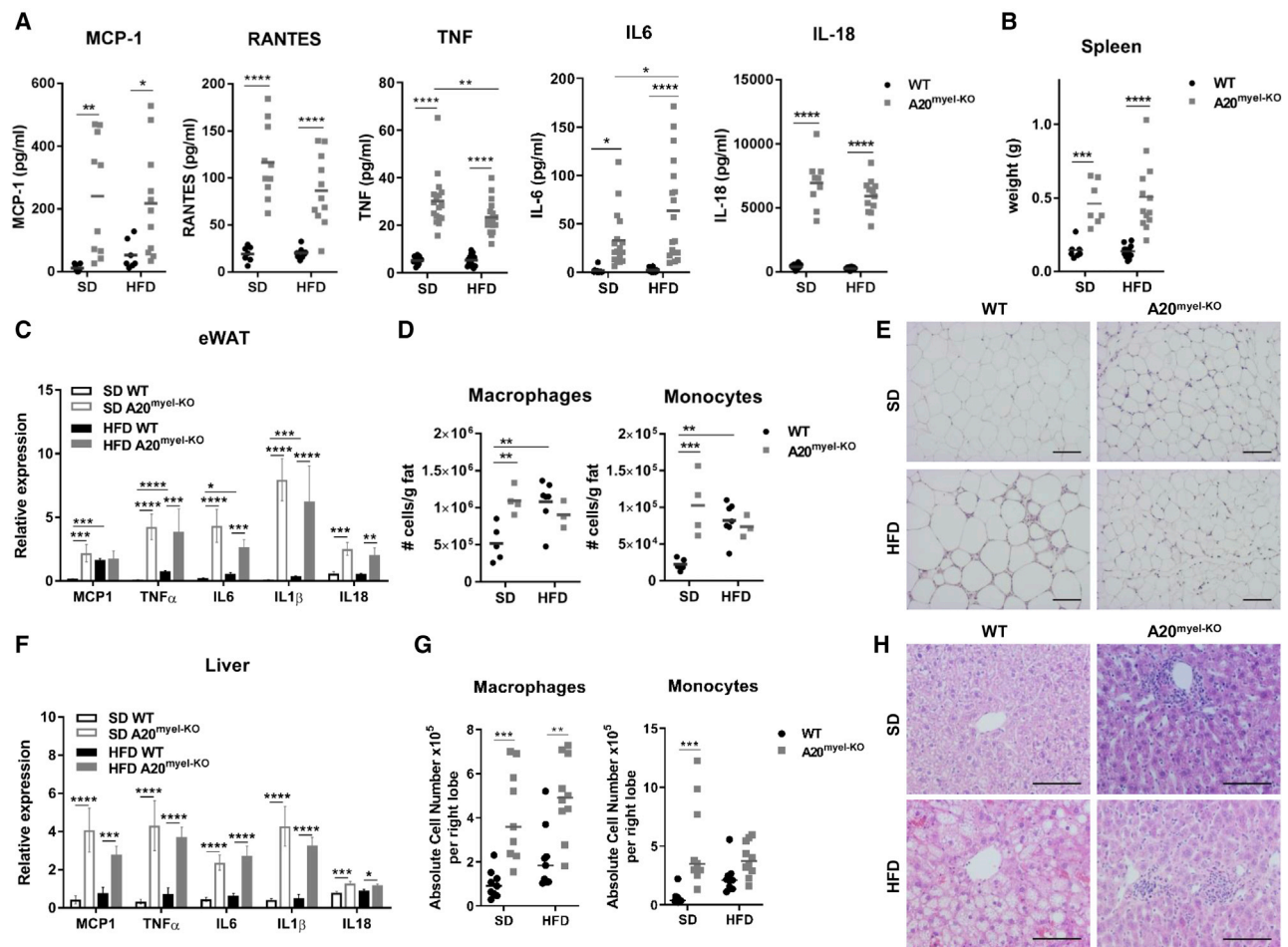
Figure 1. A20^myel-KO mice have an inflammatory condition in their metabolic tissues

(A) Levels of pro-inflammatory cytokines measured in the serum of A20^myel-KO and wild-type (WT) control mice fed with the respective diet for 12 weeks (n = 8-18).

(B) Spleen weight of A20^myel-KO and WT control mice measured after 12 weeks of diet (n = 6-14).

(C) Relative expression of pro-inflammatory genes measured by qPCR on epididymal white adipose tissue (eWAT) lysates from A20^myel-KO and WT control mice after 12 weeks of diet (n = 4-8).

(D) Quantification of the absolute number of macrophages (F4/80^+CD64^+) and recruited monocytes (Ly6C^+) by flow cytometry in eWAT from A20^myel-KO and WT control mice after 12 weeks of diet.

(E) Representative hematoxylin and eosin staining of eWAT from A20^myel-KO and WT control mice isolated after 12 weeks of diet. Scale bar, 50 μm.

(F) Relative expression of pro-inflammatory genes measured by qPCR on liver lysates from A20^myel-KO and WT control mice after 12 weeks of diet (n = 7–11).

(G) Quantification of the absolute number of macrophages (F4/80^+CD64^+) and recruited monocytes (Ly6C^+) by flow cytometry in liver from A20^myel-KO and WT control mice after 12 weeks of diet.

(H) Representative hematoxylin and eosin staining of liver from A20^myel-KO and WT control mice isolated after 12 weeks of diet. Scale bar, 100 μm.

Data are represented as mean ± SEM; ns, non-significant (p > 0.05); *p ≤ 0.05; **p ≤ 0.01; ***p ≤ 0.001; ****p ≤ 0.0001.

the role of resident ATMs versus infiltrating macrophages in the protection of A20^myel-KO mice from diet-induced obesity, we generated A20-CCR2^myel-DKO mice lacking both A20 and the chemokine receptor CCR2 in the myeloid cell compartment. Since CCR2 signaling is essential for myeloid cell recruitment into the adipose tissue (Kanda et al., 2006; Weisberg et al., 2006), this approach allowed us to investigate the importance of the resident ATM population in the metabolic phenotype observed in A20^myel-KO mice. Since A20-CCR2^myel-DKO mice are also protected from HFD-induced obesity, this demonstrates that A20 deficiency in the resident ATMs is responsible for resistance to obesity (Figures S2A and S2B).

Myeloid A20 deficiency protects mice from diet-induced insulin resistance

Given the lean phenotype of A20^myel-KO mice and the well-known association between obesity and insulin resistance, we next analyzed glucose metabolism in A20^myel-KO mice and control wild-type littermates. Hyperglycemia is significantly reduced in A20^myel-KO mice compared to control mice after the HFD (Figure 3A). Also, neither hyperinsulinemia nor hyperleptinemia develops in A20^myel-KO mice in contrast to control mice fed with the HFD (Figure 3A). When subjected to an intraperitoneal glucose tolerance test (ipGTT), wild-type mice show severe glucose intolerance accompanied by an exacerbated insulin
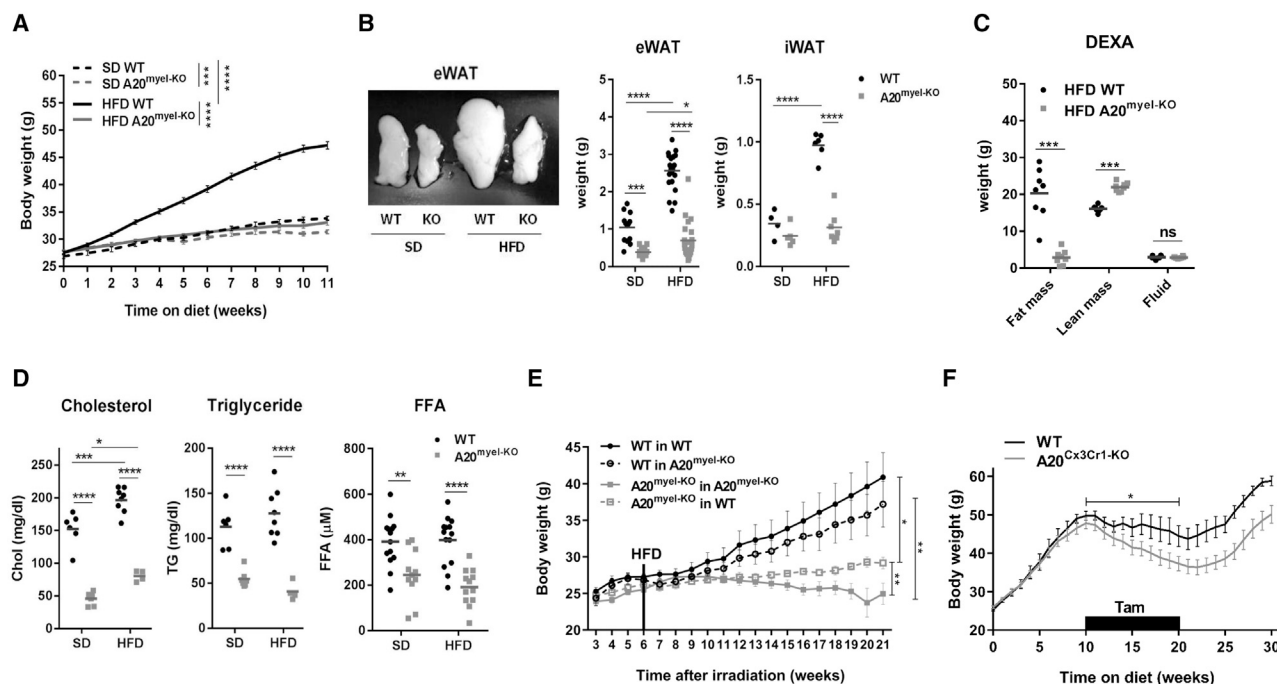
Figure 2. A20^myel-KO mice are protected from diet-induced obesity

(A) A20^myel-KO mice and control WT littermates were fed with a standard diet (SD, n = 38–39) or high fat diet (HFD, n = 53–55) for 11 weeks, and body weight was followed over time.

(B) Representative image of eWAT, and weight of eWAT (SD n = 13–16; HFD n = 23–24) and iWAT (SD n = 4–5; HFD n = 6–7) of A20^myel-KO and control WT littermate mice after 12 weeks on SD or HFD.

(C) DEXA-scan of A20^myel-KO and control WT littermate mice fed with a HFD for 5 weeks (n = 7–8).

(D) Cholesterol, triglyceride (SD n = 6–7; HFD n = 4–8), and free fatty acid (FFA) (SD n = 11–14; HFD n = 12–14) levels measured in blood serum of A20^myel-KO and control WT littermate mice after 12 weeks of diet.

(E) Body weight after bone marrow transfer of WT or A20-deficient bone marrow into irradiated WT or A20^myel-KO mice, fed with HFD 6 weeks after the irradiation (n = 4–6).

(F) Body weight of WT and A20^Cx3Cr1-KO mice on the HFD. After 10 weeks of HFD, A20 deletion was induced during 10 weeks by injecting tamoxifen subcutaneously twice a week. Thereafter, mice were kept on the HFD for another 10 weeks in the absence of tamoxifen (n = 5–8).

Data are represented as mean ± SEM; ns, non-significant; p > 0.05; *p ≤ 0.05; **p ≤ 0.01; ***p ≤ 0.001; ****p ≤ 0.0001.

response after the HFD, but A20^myel-KO mice display normal glucose and insulin responses, similar to mice fed with the SD (Figure 3B). Similarly, wild-type mice fed with the HFD develop systemic insulin resistance, while A20^myel-KO mice are completely protected and respond normally to insulin after the HFD (Figure 3C).

We previously demonstrated that A20-deficient macrophages show an exacerbated inflammatory response and constitutively produce TNF and IL-6 (Matmati et al., 2011). As a consequence, A20^myel-KO mice develop a severe erosive polyarthritis which is dependent on RIPK3-dependent macrophage necroptosis and NLRP3 inflammasome activation (Matmati et al., 2011; Polykratis et al., 2019; Vande Walle et al., 2014). To evaluate the metabolic response of A20^myel-KO mice to the HFD in conditions where the systemic inflammation is suppressed, A20^myel-KO mice were crossed to *Nlrp3* and *Ripk3* knockout mice, and A20^myel-KO NLRP3^−/− and A20^myel-KO RIPK3^−/− mice were subjected to HFD-induced obesity. However, these mice still show the protection from diet-induced obesity and insulin resistance similar to what is seen in A20^myel-KO mice (Figures S2C and S2D). Liver and

eWAT from A20^myel-KO RIPK3^−/− mice look identical to that of A20^myel-KO mice after 10 weeks on the HFD. eWAT from A20^myel-KO RIPK3^−/− mice shows the presence of infiltrating cells, but the adipocytes are much smaller than the adipocytes from wild-type and RIPK3^−/− mice challenged with the HFD. Moreover, the typical CLSs, formed by infiltrating macrophages accumulating around dead adipocytes and evident in the eWAT from wild-type and RIPK3^−/− mice after the HFD, are largely absent in the eWAT from both A20^myel-KO and A20^myel-KO RIPK3^−/− mice (Figure S2E). Also, liver tissue from A20^myel-KO and A20^myel-KO RIPK3^−/− mice looks similar after the HFD, demonstrating the presence of inflammatory foci mainly around the blood vessels but not the prominent inflammation, hepatocyte ballooning, and vacuoles of accumulated fat, reminiscent of steatohepatitis seen in liver tissue of wild-type and RIPK3^−/− mice after the HFD (Figure S2F). Together, these data demonstrate that the metabolic tissues of A20^myel-KO RIPK3^−/− mice are still inflamed, but do not show the typical hallmarks of obesity-associated inflammation, in agreement with the fact that these mice are protected from diet-induced obesity and insulin resistance.
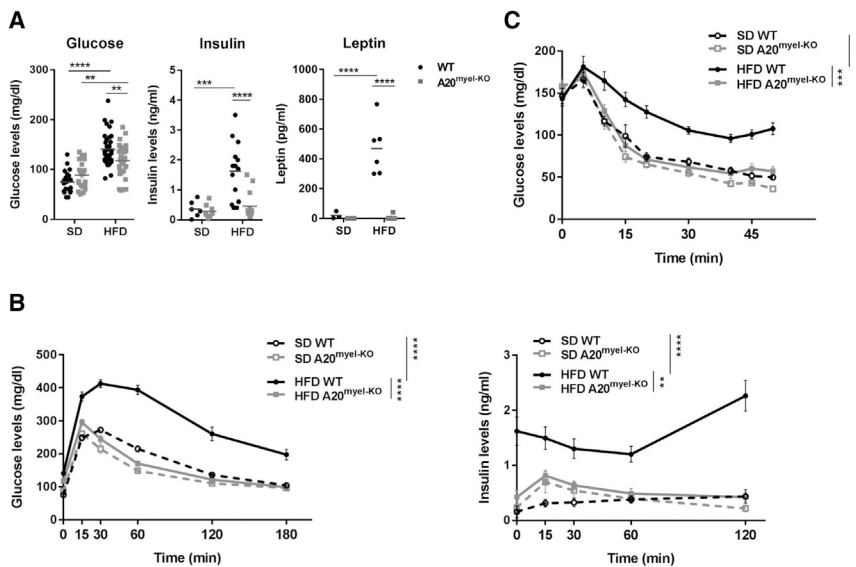
Figure 3. A20^myel-KO mice show improved glycemic control when fed with a HFD

(A) Glucose (SD n = 21–23; HFD n = 32–36), insulin (SD n = 10; HFD n = 14) and leptin (SD n = 3–4; HFD n = 9–10) levels were measured in blood after overnight starvation of A20^myel-KO and control WT mice fed with the respective diets for 10 weeks.

(B) Intraperitoneal glucose tolerance test performed on A20^myel-KO and control WT mice after 10 weeks of diet. Glucose (SD n = 21–23; HFD n = 32–36) and insulin (SD n = 8–10; HFD n = 14) levels were measured from blood at given time points after injection of glucose.

(C) Insulin tolerance test performed on A20^myel-KO and control WT mice after 11 weeks of diet, measuring glucose levels from blood at given time points after injection of insulin (SD n = 6–7; HFD n = 5–7).

Data are represented as mean ± SEM; ns, non-significant; p > 0.05; *p ≤ 0.05; **p ≤ 0.01; ***p ≤ 0.001; ****p ≤ 0.0001.
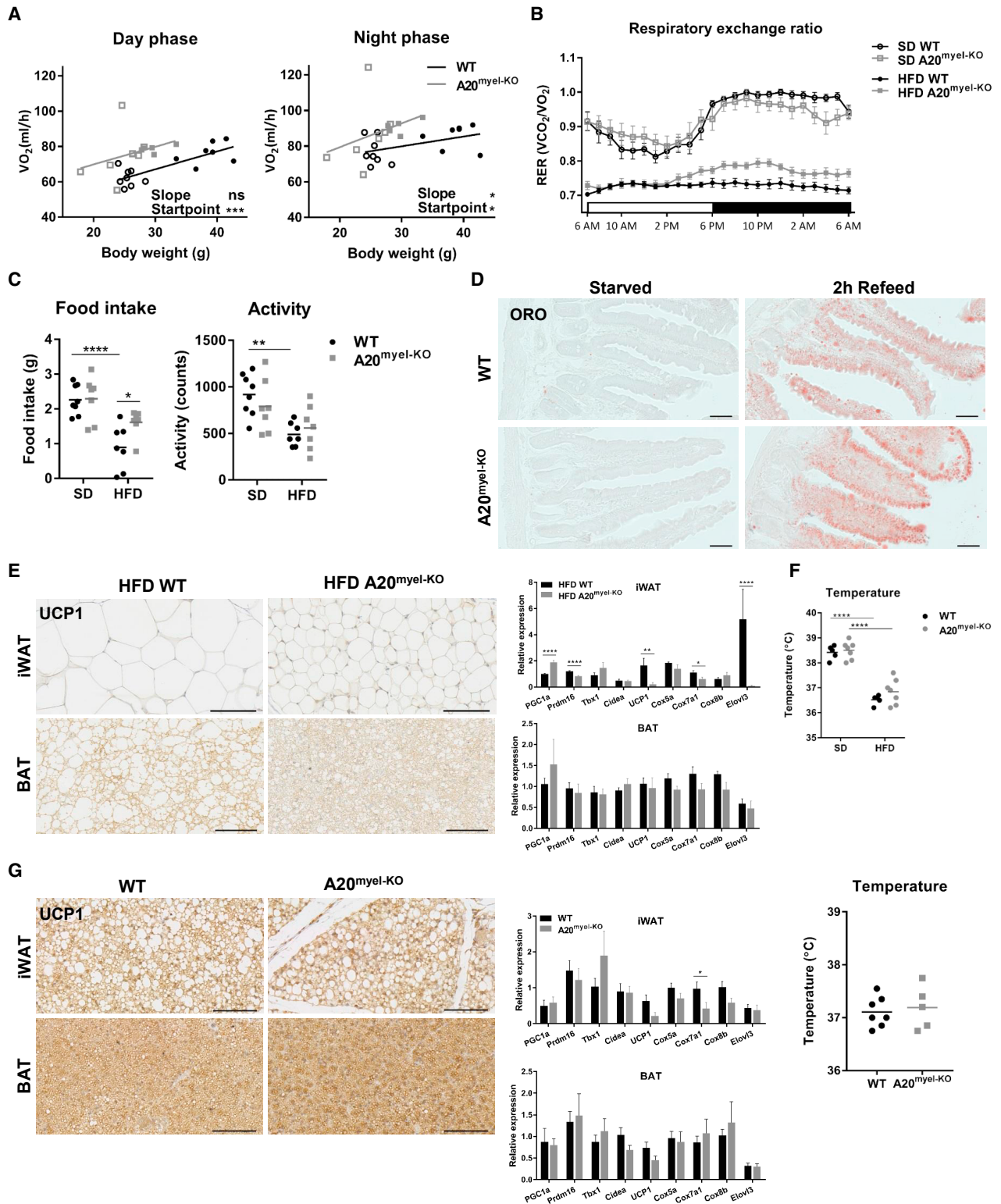
Systemic treatment of A20^myel-KO mice with TNF- or IL6-neutralizing antibodies also does not revert the phenotype (Figures S2G and S2H). Finally, since A20^myel-KO mice were shown to have an enhanced activation of adaptive immune cells (Matmati et al., 2011), we evaluated whether T and B lymphocytes are involved in the protection from diet-induced obesity in myeloid A20 knockout mice by crossing these mice with RAG2-deficient mice lacking functional T and B cells (Shinkai et al., 1992). Double homozygous A20^myel-KO RAG2^−/− mice still show protection from HFD-induced obesity (Figure S3), indicating that T and B cells are not responsible for the protection against obesity.

Myeloid A20 knockout mice consume more oxygen but have normal thermogenesis

To investigate the metabolic behavior of A20^myel-KO and control wild-type littermate mice in more detail, we measured metabolic rates of both genotypes by indirect calorimetry using metabolic chambers before and after 5 weeks of HFD. When control wild-type mice gain weight, their oxygen consumption increases (Figure 4A), confirming previous findings (Tschöp et al., 2011). Interestingly, A20^myel-KO mice have an even higher oxygen consumption, despite their leaner body composition, especially in the night phase when mice are more active (Figure 4A). The respiratory exchange ratio (RER), the ratio between the amount of carbon dioxide (VCO_2) produced and oxygen (VO_2) consumed during metabolism, gives an indication of the fuel source used to generate energy. Mice fed with the SD have an RER around 1, indicating their use of carbohydrates as a fuel source (Figure 4B). On the HFD, control mice predominantly use fat as a fuel source, lowering the RER to 0.7. However, A20^myel-KO mice show a higher RER in the night phase, indicating that they use a mix of fat and carbohydrates as a fuel source (Figure 4B). Also, A20^myel-KO mice consume even more food than control wild-type mice when fed the HFD, but no difference in locomotor activity can be observed between both groups of mice

(Figure 4C). To check if the A20^myel-KO mice take up the lipids from the HFD, mice were starved overnight and refed for two hours, after which the small intestine was stained for presence of lipid droplets. Oil red O staining demonstrated that A20^myel-KO mice take up lipids from the diet to the same extent as wild-type littermates (Figure 4D). Together, these data indicate that the protective lean phenotype of A20^myel-KO mice is not due to reduced food intake, increased activity, or malabsorption of the diet. Instead, A20^myel-KO mice have a higher metabolic rate compared with control mice.

Protection against HFD-induced obesity is often explained by increased thermogenesis, which can be monitored by assessing the activity of uncoupling protein 1 (UCP1), the protein responsible for maintaining core body temperature and regulating body weight by increasing whole-body energy expenditure (Brestoff and Artis, 2015; Rosen and Spiegelman, 2014). However, no increased UCP1 staining nor increased expression of genes involved in thermogenesis could be observed in brown adipose tissue (BAT), the primary organ responsible for thermogenesis, of A20^myel-KO mice after the HFD (Figure 4E). Next to BAT, thermogenesis can also occur in the inguinal fat pad (iWAT) due to the transformation of white adipocytes into brown or "beige" adipocytes (Rosen and Spiegelman, 2014). However, no staining for UCP1 or increased gene expression could be detected in iWAT of A20^myel-KO mice (Figure 4E). Also, no difference in heat production, an indirect measure of thermogenesis, could be observed between wild-type and A20^myel-KO mice after the HFD (Figure 4F). As thermogenesis is also dependent on the fat composition of the body, these experiments were repeated on lean, weight-matched, and individually housed wild-type and A20^myel-KO mice. However, no differences in expression of thermogenic markers, UCP1 staining of fat tissue, or body temperature could be observed between wild-type and A20^myel-KO littermate mice (Figure 4G), indicating that the absence of A20 in myeloid cells does not influence thermogenesis.

A

Day phase / Night phase (VO₂ ml/h vs Body weight)

B Respiratory exchange ratio

C Food intake / Activity

D Starved / 2h Refeed (ORO)

E HFD WT / HFD A20^myel-KO (UCP1, iWAT/BAT); iWAT/BAT relative expression

F Temperature

G WT / A20^myel-KO (UCP1, iWAT/BAT); iWAT/BAT relative expression; Temperature

(legend on next page)

Myeloid A20 deficiency promotes the expansion of highly inflammatory CD206+ ATMs

During obesity, the adipose tissue becomes infiltrated with pro-inflammatory CD11c^{+} macrophages that form characteristic CLSs around dying adipocytes (Osborn and Olefsky, 2012). In contrast, a lean state is associated with anti-inflammatory CD206^{+} macrophages that reside interstitially between adipocytes to maintain adipose tissue homeostasis (Osborn and Olefsky, 2012). Histology on fat tissue indeed shows the presence of CLS in eWAT of wild-type mice on the HFD, but this is strongly reduced in A20[myel-KO] mice (Figure 1E). However, flow cytometry of eWAT reveals that, despite their protected phenotype in obesity and insulin resistance, A20[myel-KO] mice display clear signs of eWAT inflammation, characterized by high numbers of macrophages and infiltrating monocytes, similar to the levels seen in the HFD wild-type mice (Figure 1D). The number of eosinophils was reduced in eWAT of A20[myel-KO] mice, while the number of granulocytes was higher, although to a much lower extent than the macrophage population (Figure S4). Further characterization of the eWAT-associated ATMs identified predominantly CD11c^{low} CD206^{+} macrophages in A20[myel-KO] mice, while wild-type control mice fed with the HFD predominantly accumulate CD206^{low} CD11c^{+} macrophages (Figures 5A and 5B). Interestingly, although ATMs from A20[myel-KO] mice show the same polarization as their lean counterparts, the absolute number of CD206^{+} macrophages is higher (Figure 5A). The CD11c^{+} macrophages mainly localize to CLSs around the dying adipocytes, which is evident in obese wild-type mice fed the HFD (Figure 5C). On the contrary, CD206^{+} macrophages localize interstitially between adipocytes, as demonstrated in eWAT of A20[myel-KO] mice and in control mice fed with the SD (Figure 5C).

To further investigate the function of the different macrophage populations in SD- and HFD-fed control and A20[myel-KO] mice, RNA sequencing (RNA-seq) was performed on fluorescence-activated cell sorting (FACS)-purified CD206^{+} and CD11c^{+} ATM subclasses isolated from eWAT of A20[myel-KO] and wild-type mice. Clustering analysis shows that ATMs isolated from A20[myel-KO] eWAT display a different gene expression pattern compared to wild-type ATMs, and this difference is already obvious in the lean condition (Figure 5D). Interestingly, A20[myel-KO] ATMs cluster together regardless of the diet (Figure 5D), and no genes are differentially regulated in each ATM subclass between the two diets in the absence of A20. This indicates that despite a similar lean body composition, there is an intrinsic difference between wild-type ATMs from mice fed with

the SD and A20-deficient ATMs. Furthermore, CD11c^{+} and CD206^{+} macrophages are clearly separated in all conditions and are different between diets. Only the CD11c^{+} ATM population from wild-type HFD mice displays a more intermediate phenotype (Figure 5D), which is indicative of an ongoing polarization from a CD206^{high}CD11c^{low} state to a CD206^{low}CD11c^{high} state. IPA (Ingenuity Pathway Analysis) revealed that the gene pathways that show the most prominent differences between A20-deficient ATMs and wild-type ATMs are typical pro-inflammatory pathways, a signature which is independent of the CD11c^{+} or CD206^{+} classification and of the diet and is solely determined by the absence of A20 (Figure 5E; Figure S5A). Interestingly, A20-deficient ATMs have a higher expression of genes normally associated with obese ATMs (Nos2, Il6, Il12b, Ifng), despite being completely protected from HFD-induced obesity (Figure 5F; Figure S5B). Together, these data indicate that A20[myel-KO] mice have elevated numbers of mainly CD206^{+} ATMs. ATMs deficient of A20 display a general transcription profile similar to their lean wild-type counterparts based on the CD206^{+} and CD11c^{+} classification, but also have a pro-inflammatory signature, regulated by IFNγ and LPS, that is independent of the diet and is not present in wild-type ATMs.

Absence of A20 in macrophages leads to upregulation of Irg1 and increased palmitate consumption in vitro and in vivo

Analysis of the RNA-seq data demonstrated that immune responsive gene 1 (Irg1, also known as Acod1), is the second most highly upregulated gene between A20-deficient and wild-type ATMs (Figures S5C, S5D, and S6A). Irg1 is one of the highest upregulated genes in macrophages when stimulated in vitro with pro-inflammatory components such as LPS (lipopolysaccharide) and IFNγ (Degrandi et al., 2009; Strelko et al., 2011). Irg1 uses the tricarboxylic acid (TCA) cycle intermediate cis-aconitate to produce itaconic acid. Indeed, A20[myel-KO] mice show elevated levels of itaconic acid in their adipose tissue, and levels of itaconic acid are also increased in the serum of these mice (Figure S6B). Itaconic acid was recently identified as one of the key metabolites regulating the TCA cycle and the metabolic switch to aerobic glycolysis upon activation in macrophages (O'Neill and Artyomov, 2019). Therefore, we performed ^{13}C tracing experiments to further investigate the metabolism of A20-deficient macrophages using ^{13}C labeled glucose, glutamine, and palmitate (Figure 6A). The different tracers enter the TCA cycle and incorporate into the carbons of several

---

Figure 4. A20[myel-KO] mice show increased oxygen consumption but not increased thermogenesis

A20[myel-KO] and WT control mice were analyzed by indirect calorimetry in individually housed metabolic cages, where the same mice were measured before and after 5 weeks of the HFD (n = 5–8).

(A and B) Oxygen consumption compared to body weight (A) and respiratory exchange ratio (VCO$_2$/VO$_2$) (B) were measured on the same mice before HFD and after 5 weeks of the HFD.

(C) Food intake and activity were monitored by individual housing of mice in metabolic cages before and after 5 weeks of the HFD.

(D) Oil red O staining of the small intestine of WT and A20[myel-KO] mice after overnight starvation and a two hour refeed with HFD. Scale bar, 50 μm (n = 3–4).

(E) Representative image of UCP1 staining of iWAT and BAT. Scale bar, 100 μm (n = 7–9), and relative expression of thermogenic genes measured by qPCR on iWAT and BAT lysates (n = 4–6) after 12 weeks of the HFD.

(F) Rectal body temperature of WT and A20[myel-KO] mice after individual housing for 3 days, 2 weeks after SD and 10 weeks after HFD (n = 5–7).

(G) Representative image of UCP1 staining of iWAT and BAT (scale bar, 100 μm), relative expression of thermogenic genes measured by qPCR on iWAT and BAT lysates, and rectal body temperature of weight-matched WT and A20[myel-KO] mice (n = 5–7) after single housing and the SD/HFD.

Data are represented as mean ± SEM; ns, non-significant; p > 0.05; *p ≤ 0.05; **p ≤ 0.01; ***p ≤ 0.001; ****p ≤ 0.0001.

A CD206^high^ CD11c^low^

B

C

D

E

Upstream regulators	CD11c+ SD WT vs A20^myel-KO		CD206+ SD WT vs A20^myel-KO		CD11c+ HFD WT vs A20^myel-KO		CD206+ HFD WT vs A20^myel-KO	
	Z	p	Z	p	Z	p	Z	p
IFNγ	8,29	64,20	8,52	52,87	9,86	68,57	8,65	56,57
IRF7	7,10	37,94	7,55	31,30	7,54	29,60	7,54	38,11
Poly rI:rC-RNA	6,53	41,84	7,70	30,79	7,69	35,33	7,74	32,74
LPS	8,38	77,14	6,79	66,34	7,30	78,00	6,18	65,12
STAT1	6,63	44,87	7,12	36,26	6,67	37,82	6,68	41,08
IRF3	6,38	36,46	6,02	32,39	6,23	28,03	6,37	32,59
IFNα	6,03	35,50	5,72	24,80	6,31	25,78	6,44	25,77
Ifnar	5,35	38,03	5,98	31,83	6,10	35,55	6,12	38,72
TLR4	5,70	34,42	5,19	27,43	5,48	29,61	5,79	25,59
MYD88	5,41	26,67	5,09	24,59	5,45	23,45	4,98	21,98
TNF	5,14	47,55	5,79	50,53	5,41	55,76	4,00	51,20

F

Figure 5. A20^myel-KO mice display an increase of inflammatory CD206+ macrophages in their adipose tissue
(A and B) Quantification of the number of CD11c+ macrophages (CD206^low^CD11c^high^) and CD206+ macrophages (CD206^high^CD11c^low^) by flow cytometry on eWAT of WT and A20^myel-KO mice after 12 weeks of the SD or HFD.
(C) Representative immunofluorescence microscopy images staining CD11c (green) and CD206 (red) on whole mount sections of eWAT of WT and A20^myel-KO mice after 12 weeks of the SD or HFD. Scale bar, 100 μm.

(legend continued on next page)

metabolites. As the TCA cycle turns multiple rounds, the labeling will accumulate at the different carbon positions. Bone-marrow-derived macrophages (BMDMs) from wild-type and A20$^{myel-KO}$ mice, unstimulated or stimulated with LPS and IFNγ, were cultured for 48 hours in the presence of ^{13}C labeled glucose, glutamine, or palmitate, and tracer incorporation was monitored in metabolites of the glycolysis and TCA using mass spectrometry. No differences in fractional contribution were found in the glycolysis pathway between wild-type and A20-deficient BMDMs (data not shown). Unstimulated wild-type and A20 knockout BMDMs, pulsed with ^{13}C glucose, showed label incorporation in TCA cycle intermediates (albeit to different extents) (Figure 6B, first row). However, under stimulated conditions, TCA cycle intermediates of either wild-type or A20 knockout BMDMs did not get labeled. Rather, under stimulated conditions, glucose labeling was found to provide mainly an m2 isotopologue of citrate (m2). This indicates that the flux of labeled carbons from glucose into the remaining TCA cycle intermediates was most likely interrupted, and that the majority of the cis-aconitate was being converted into itaconic acid, as can be observed by the high label incorporation in itaconic acid (Figure 6B, first row). The observed flux diversion, leading to depleted *de novo* label incorporation in the TCA cycle intermediates, prompted us to analyze if, under stimulated conditions, anaplerotic reactions compensate for the loss of flux into the TCA cycle. We labeled cells with ^{13}C-glutamine and found an enhanced flux into the TCA cycle intermediates such as α-ketoglutaric acid, fumaric acid, and malic acid under stimulated conditions for both wild-type and A20 knockout BMDMs (Figure 6B, second row).

Since in unstimulated A20 knockout BMDMs the fraction labeling of citrate was lower compared to wild-type BMDMs, and the labeling in itaconic acid was comparable between both, this indicates that A20-deficient cells most likely rely on another substrate source to produce the observed higher levels of itaconic acid (Figure 6B, first row). This difference cannot be explained by the contribution of glutamine, as a similar glutamine-derived labeling pattern is seen between wild-type and A20 knockout cells (Figure 6B, second row). Interestingly, A20 knockout cells show a significant increase of palmitate contribution into citrate and itaconic acid, especially under stimulated conditions, indicating that they switch to palmitate oxidation to produce itaconic acid, in contrast to wild-type cells that use mainly glucose and glutamine for the synthesis of itaconic acid (Figure 6B, third row). Given this high palmitate labeling in itaconic acid, this suggests that A20 macrophages use palmitate to make itaconic acid, which could explain why the A20$^{myel-KO}$ mice are protected from HFD-induced obesity.

To investigate if the higher levels of itaconate observed in A20$^{myel-KO}$ mice provide protection from HFD-induced obesity, mice were crossed with either floxed *Irg1* mice (Nair et al., 2018) to generate A20$^{myel-KO}$-Irg1 double knockout (A20$^{myel-KO}$Irg1$^{myel-KO}$) mice or with full *Irg1* knockout (A20$^{myel-KO}$Irg1$^{-/-}$) mice. However, these double knockout mice were still protected from HFD-induced obesity to the same extent as the A20$^{myel-KO}$ mice, demonstrating that additional Irg1 deletion could not rescue the lean phenotype of A20$^{myel-KO}$ mice (Figures S6C and S6D). Deletion of Irg1 and A20 was confirmed by qPCR on cultured peritoneal macrophages stimulated with IFNγ and LPS (Figure S6E). Circulating levels of itaconic acid are significantly lower in A20$^{myel-KO}$Irg1$^{myel-KO}$ mice compared to the levels in A20$^{myel-KO}$ mice, but still higher than the levels measured in the serum of control wild-type mice (Figure S6F), questioning the source of the remaining itaconic acid. As the activation status and corresponding metabolism of macrophages is highly dependent on the surrounding microenvironment and difficult to recapitulate *ex vivo*, we next performed an *in vivo* ^{13}C palmitate labeling experiment. Wild-type and A20$^{myel-KO}$ mice were injected with 3 μmol ^{13}C palmitate dissolved in 1.2% lecithin/2.5% glycerol (^{13}C PA) or with 1.2% lecithin/2.5% glycerol alone, after which tracer metabolomics was performed on thioglycollate-elicited peritoneal fluid. The major drawback of *in vivo* metabolomics is the limited time frame between cell isolation and metabolite extraction. Therefore, we opted for thioglycollate-elicited peritoneal fluid since it contains a large macrophage population that can be quickly isolated (Figure S7). Labeling by ^{13}C palmitate can be found in multiple metabolites, confirming efficient labeling (Figure 7A). Interestingly, A20$^{myel-KO}$ mice show significantly more palmitate labeling in citric acid and especially in itaconic acid but also in metabolites downstream of itaconic acid such as fumaric acid and malic acid (Figure 7A). These data indicate that macrophages from A20$^{myel-KO}$ mice have a preference to metabolize palmitate to fuel their metabolic flux also *in vivo*. To confirm, we assessed fatty acid uptake on macrophages isolated from different organs by using Bodipy-palmitate, a fluorescently tagged form of palmitic acid that allows us to monitor cellular fatty acid uptake (O'Sullivan et al., 2014). This demonstrates a stronger uptake of palmitate by macrophages in liver and spleen from A20$^{myel-KO}$ mice compared to the uptake in wild-type mice (Figure 7B). In eWAT, a stronger uptake could be observed in A20$^{myel-KO}$ macrophages but only in SD conditions. These data are in line with the RNA-seq analysis (Figures 5D–SF), revealing strong differences in gene expression in eWAT macrophages derived from wild-type and A20$^{myel-KO}$ mice already in SD conditions, showing that the phenotype is readily apparent in baseline.

(D) RNA sequencing and cluster analysis on CD11c$^+$ (CD206^{low}CD11c^{high}) and CD206$^+$ (CD206^{high}CD11c^{low}) adipose tissue macrophages (ATMs) sorted from eWAT of WT and A20$^{myel-KO}$ mice after 12 weeks of the SD or HFD (n = 4 per genotype).

(E) Table of top differentially regulated gene networks comparing gene expression from RNA sequencing data between A20$^{myel-KO}$ and control WT CD11c$^+$ and CD206$^+$ ATMs after 12 weeks of the SD or HFD using IPA software (n = 4). z = Z score, p = overlap p value (-log(p value)).

(F) Heatmap showing the expression levels of pro- and anti-inflammatory markers associated with obese CD11c$^+$ and lean CD206$^+$ ATMs from RNA sequencing data obtained from A20$^{myel-KO}$ (n = 4) and control (n = 4) WT CD11c$^+$ and CD206$^+$ ATMs after 12 weeks of the SD or HFD. Upregulated genes (red), downregulated genes (blue).

Data are represented as mean $\pm$ SEM; **$p \leq 0.01$; ****$p \leq 0.0001$.
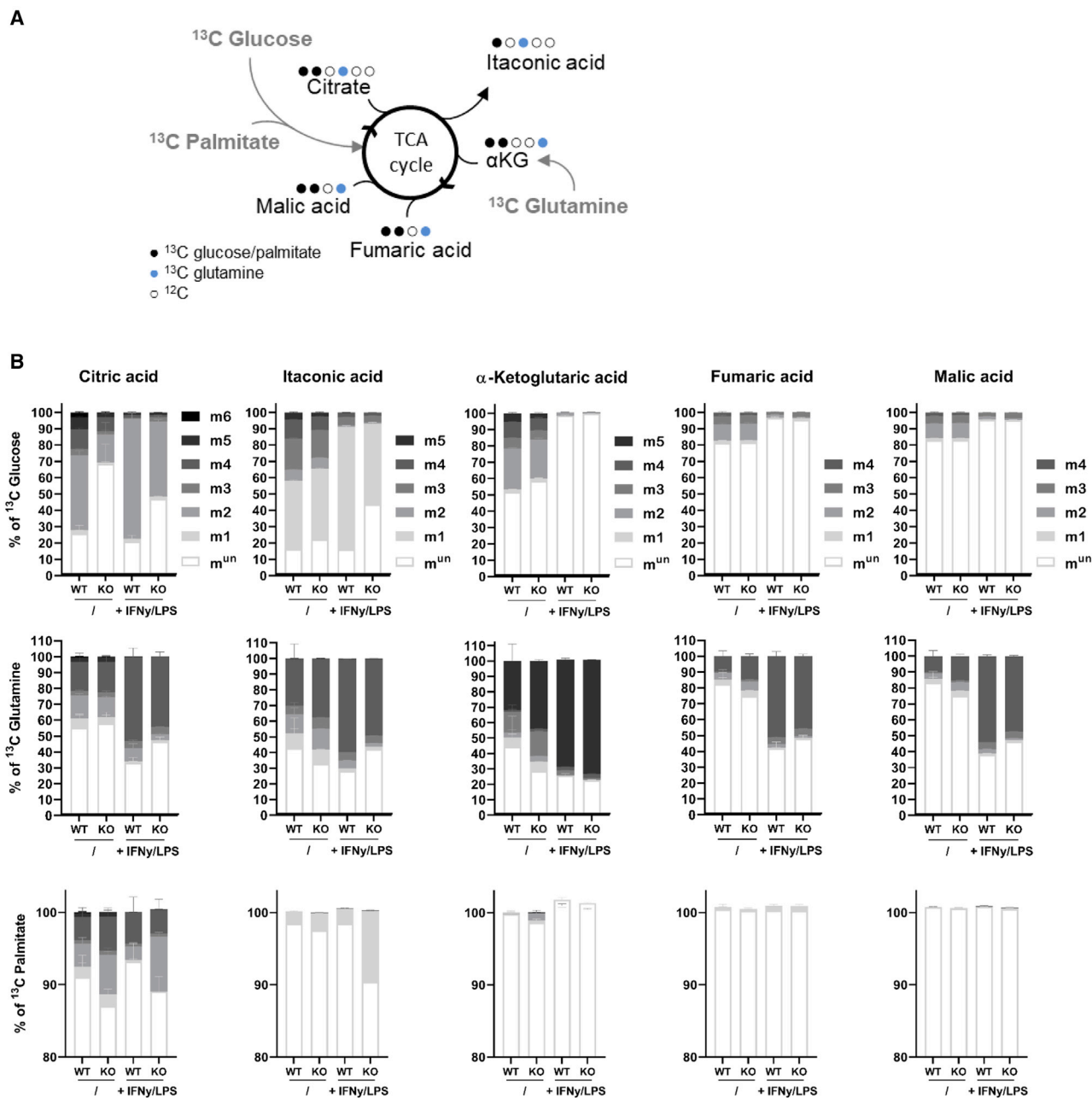
Figure 6. A20-deficient macrophages have a preference to metabolize palmitate *in vitro*

(A) Scheme explaining ^{13}C metabolic tracing. Labeled glucose, glutamine, or palmitate will enter the TCA cycle and label the first carbons of several metabolites. As the TCA cycle turns multiple cycles, the labeling will accumulate in the different carbon positions.

(B) WT or A20 knockout (KO) BMDMs were left untreated or stimulated with LPS/IFNγ (10ng/ml) and cultured for 48 hours with medium containing ^{13}C labeled glucose, glutamine, or palmitate, after which the metabolites were analyzed for the tracer using mass spectrometry (n = 3). (m^{un}), unlabeled carbon; (m$^{1-6}$), the first through sixth carbon position in a metabolite.

To evaluate whether A20 deficiency affects mitochondrial function and biogenesis in macrophages, we performed an extracellular flux analysis in both BMDMs and in immortalized monocyte/macrophage HoxB8 progenitor cells derived from wild-type and A20$^{myel-KO}$ mice. Compared to wild-type macrophages, A20-deficient macrophages exhibit a strong and signif-

icant reduction in baseline oxygen consumption rate (OCR). This difference is even more pronounced after carbonyl cyanide p-(tri-fluoromethoxy)phenyl-hydrazone (FCCP)-induced uncoupling during OXPHOS (oxidative phosphorylation), as shown by OCR and spare respiratory capacity (SRC), demonstrating that the A20 knockout cells have a reduced ability to increase their
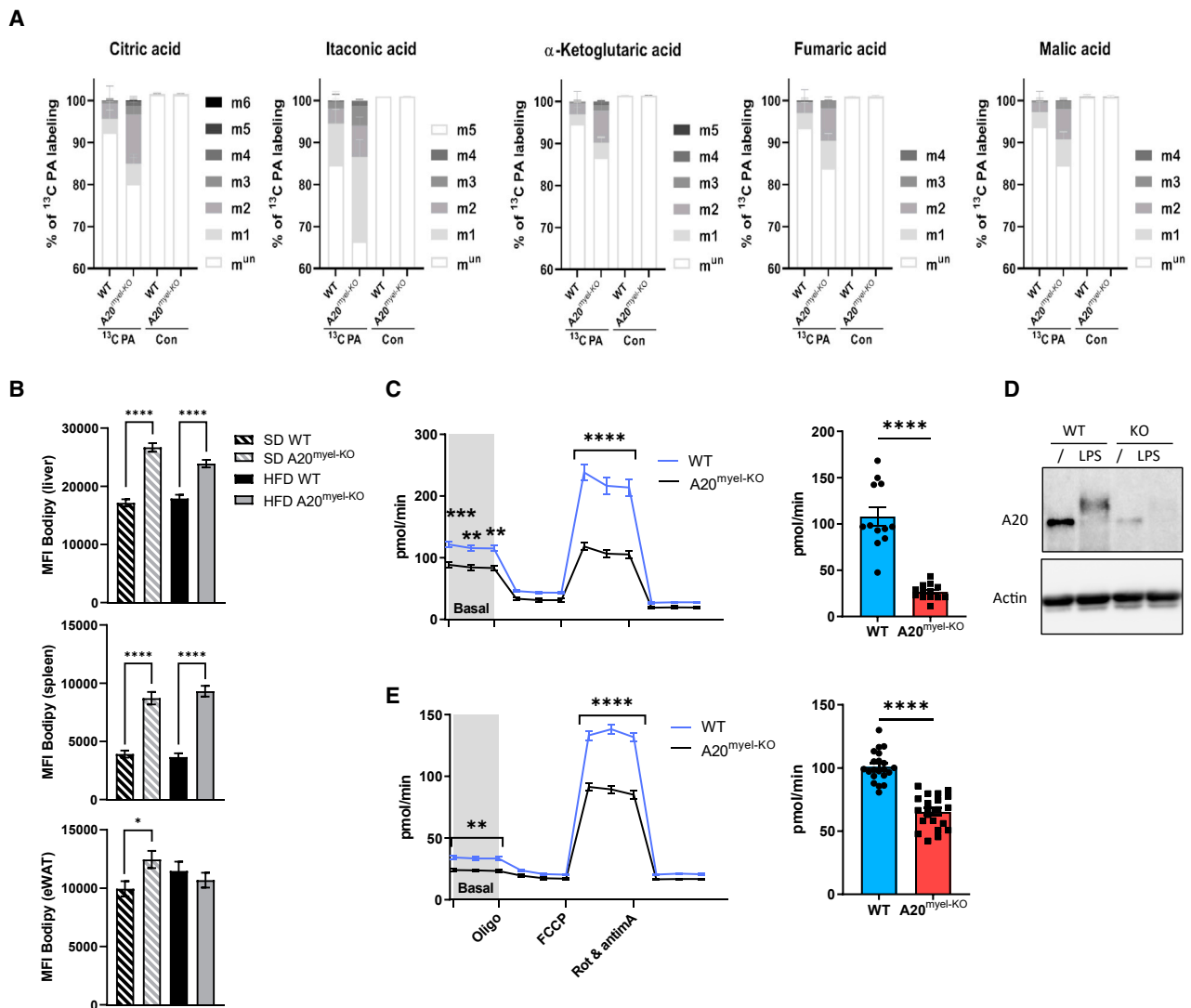
Figure 7. A20-deficient cells have a preference to metabolize palmitate *in vivo*

(A) WT and A20$^{myel-KO}$ mice were injected with 3 μmol ^{13}C palmitate dissolved in 1.2% lecithin/2.5% glycerol (^{13}C PA) or with 1.2% lecithin/2.5% glycerol alone (Con) 4 hours before thioglycolate-elicited peritoneal fluid was isolated and analyzed for the tracer using mass spectrometry (n = 5–7 ^{13}C PA; n = 3–4 Con). (m^{un}), unlabeled carbon; (m$^{1-6}$), the first through sixth carbon position in a metabolite. Data are represented as mean ± SEM; ns, non-significant; p > 0.05; *p ≤ 0.05; **p ≤ 0.01; ***p ≤ 0.001; ****p ≤ 0.0001.

(B) Mean fluorescent intensity (MFI) as a measure for Bodipy-labeled palmitate uptake in macrophages isolated from liver, spleen, and eWAT. Data pooled from 4 experiments (n = 8–12 mice/group) and represented as mean ± SEM. *p ≤ 0.05; **p ≤ 0.01; ***p ≤ 0.001; ****p ≤ 0.0001.

(C) Real-time measurement of oxygen consumption rate (OCR, left) analyzed in WT and A20 KO HoxB8 macrophages by sequential treatment with oligomycin, FCCP, and rotenone + antimycinA, as an indicator of oxidative metabolism. Spare respiratory capacity (SRC, right) after addition of FCCP. Data pooled from 2 experiments and represented as mean ± SEM. **p ≤ 0.01; ***p ≤ 0.001; ****p ≤ 0.0001.

(D) Western blot analysis for expression of A20 in lysates from WT and A20-deficient (KO) HoxB8 cells. Anti-actin immunoblotting was used as loading control.

(E) Real-time measurement of OCR (left) analyzed in WT and A20 KO BMDM by sequential treatment with oligomycin, FCCP, and rotenone + antimycinA, as an indicator of oxidative metabolism. SRC (right) after addition of FCCP.

Data pooled from 2 experiments and represented as mean ± SEM. **p ≤ 0.01; ****p ≤ 0.0001.

energy production when using carbon sources readily available in the test medium (glucose, glutamaine, and pyruvate) (Figures 7C–7E). We also showed that the cells do not rely on intrinsic FFA oxidation, since incubation with Etomoxir, an inhibitor of carnitine palmitoyl transferase 1 (CPT1) and a rate-limiting enzyme

for beta-oxidation of fatty acids in mitochondria, does not affect OCR and SRC (Figure S8).

In conclusion, these data identify A20 as a crucial control on metabolic signaling and metabolic reprogramming in macrophages. Given the increased macrophage numbers in A20$^{myel-KO}$

mice (Figures 1D and 1G), we hypothesize that these macrophages consume a large bulk of the fatty acids present in the HFD, resulting in the protection of A20^myel-KO mice against diet-induced obesity.

DISCUSSION

In this study, we describe an important role for the NF-κB regulatory protein A20 in myeloid cells during the development of obesity. We show that absence of A20 in myeloid cells leads to a complete protection against diet-induced obesity and insulin resistance.

During obesity, adipose tissue shows a dramatic shift from a type 2 to a more type 1 cytokine-associated immune environment, where the numbers of type 2 immune cells such as regulatory T cells (Tregs) and eosinophils gradually decrease, and the numbers of lymphocytes, granulocytes, and monocytes increase. This leads to a positive feedback, resulting in a chronic low-grade inflammatory state (Lumeng et al., 2007). Macrophages are major players in this process, and ATMs are known to switch from an anti-inflammatory CD206+ state to a pro-inflammatory CD11c+ state, augmenting the inflammatory response and affecting insulin sensitivity. In addition, newly recruited CD11c+ macrophages contribute to the inflammatory response (Osborn and Olefsky, 2012). Increased numbers of CD206+ macrophages can be detected in the adipose tissue of A20^myel-KO mice, in contrast to control mice which accumulate CD11c+ ATMs upon the HFD. However, the adipose tissue of A20^myel-KO mice shows an increased expression of pro-inflammatory cytokines, and RNA-seq of A20-deficient ATMs reveals an expression pattern related to IFNγ and LPS signaling, indicative of classical M1 polarization. This suggests that A20-deficient ATMs show aspects of pro-inflammatory signaling, which is different from the gene signature of CD11c+ macrophages seen in obese control mice. More recent studies based on unbiased "omics" approaches have also shown that the profile of ATMs that accumulate during obesity is different from the profile of classically activated inflammatory macrophages and show a metabolically activated profile reminiscent of arachidonic acid metabolism, glycerolipid metabolism, lipid binding, endocytosis, and phagocytosis (Hill et al., 2018; Kratz et al., 2014; Weinstock et al., 2019; Sharma et al., 2019; Silva et al., 2019; Xu et al., 2013). In addition, it is well established that the degree of inflammation correlates with the severity of insulin resistance (Hotamisligil, 2006; Lumeng and Saltiel, 2011; Reilly and Saltiel, 2017), and inflammation can induce insulin resistance independent of obesity (Cani et al., 2007; Kanda et al., 2006). Therefore, it is surprising that A20^myel-KO mice do not develop insulin resistance, as their metabolic tissues have a pro-inflammatory signature.

The chemokine receptor CCR2 regulates monocyte and macrophage recruitment and is necessary for macrophage-dependent inflammatory responses and the development of obesity-associated adipose tissue inflammation and systemic insulin resistance (Kanda et al., 2006; Weisberg et al., 2006). Hence, Ccr2 deficiency reduces macrophage infiltration and the inflammatory profile of adipose tissue and attenuates the development of obesity in mice (Weisberg et al., 2006). In our

study, mice lacking both A20 and CCR2 in the myeloid cell compartment still show protection against diet-induced obesity and glucose intolerance, demonstrating that A20 deficiency in the resident ATMs, and not in the recruited ATMs, is responsible for the observed resistance to obesity. However, this does not exclude that other macrophages, resident in other tissues and CCR2-independent, might also contribute to the observed phenotype. This appears likely based on the effects observed in spleen and liver macrophages and might explain the systemic effects on FFAs circulating in the blood. In addition, CCR2 was shown to potentiate adipose tissue inflammation in thermoneutral-housed mice but not insulin resistance, suggesting that adipose tissue inflammation is not unequivocally coupled to insulin resistance (Tian et al., 2016). Our study indicates that our knowledge on the function of ATMs, the different ATMs subpopulations, and their respective contribution to obesity-associated inflammation is still limited. Studies using single-cell RNA-seq and other unbiased approaches could provide clarity on this matter and help redefine the hallmarks of obesity.

Clustering analysis of RNA-seq data shows that both the CD11c+ and CD206+ A20-deficient ATM populations on either diet are very different from their lean wild-type counterparts. The diet also does not affect gene expression in A20-deficient ATMs, as no genes are differentially regulated between standard and HFD in these ATM subpopulations. This shows that an intrinsic difference in A20-deficient ATMs causes the lean phenotype of A20^myel-KO mice.

Recent research has focused on the close interactions between inflammation and metabolism and has shown that especially immune cells adapt their metabolism according to their inflammatory state (Ghesquière et al., 2014). Recently, the metabolite itaconic acid was identified to be crucial in this aerobic switch, together with succinate (O'Neill and Artyomov, 2019). ATMs lacking A20 highly upregulate Irg1, the enzyme that generates itaconic acid. However, genetic deletion of Irg1 in A20^myel-KO mice could not reverse the lean phenotype. It is highly likely that there could be compensatory flux rerouting the excess of palmitate in the stable Irg1 knockout mice, leading to the maintenance of the lean phenotype. Stable knockouts of metabolic enzymes often lead to such outcomes, owing to the plasticity of metabolic networks.

We could further demonstrate that A20 plays an important role in metabolic signaling and metabolic reprogramming in macrophages by showing that A20-deficient macrophages rely more on palmitate oxidation to fuel the synthesis of itaconic acid and their metabolic flux. Since A20^myel-KO mice have low levels of FFAs and triglycerides in the serum, we hypothesize that these mice are protected from diet-induced obesity because their macrophages metabolize the fatty acids present in the diet. As a result, there is no nutritional excess, and no expansion of the adipose tissue will occur. Other studies have shown that the metabolism of macrophages can affect adiposity and responses to the HFD (Sharma et al., 2019; Wilson et al., 2018). How A20 controls fatty acid metabolism is still unclear and the subject of future research. Interestingly, an interactome analysis to find novel interaction partners of A20 identified the protein GPAT3 as an interaction partner for A20 (Eyckerman et al., 2016).

Glycerol-3-phosphate acyltransferases are the rate-limiting enzymes in fatty acid synthesis, and GPAT3 and GPAT4 knockout mice show increased energy expenditure and reduced adiposity, making this a potential candidate (Cao et al., 2014; Yu et al., 2018; Zhang et al., 2014).

In conclusion, deletion of A20 in myeloid cells leads to a complete protection from diet-induced obesity and insulin resistance, despite the presence of systemic inflammation. We speculate that the lean phenotype of A20$^{myel-KO}$ mice is caused by increased oxygen consumption and increased fatty acid metabolism of A20-deficient macrophages. However, further studies are needed to investigate the role of A20 in macrophage fatty acid metabolism in more detail.

STAR★METHODS

Detailed methods are provided in the online version of this paper and include the following:

- ● KEY RESOURCES TABLE
- ● RESOURCE AVAILABILITY
  - ○ Lead contact
  - ○ Materials availability
  - ○ Data and code availability
- ● EXPERIMENTAL MODEL AND SUBJECT DETAILS
  - ○ Animals
  - ○ Cells
- ● METHOD DETAILS
  - ○ Animals
  - ○ DEXA scan
  - ○ Analytical assays
  - ○ Assessment of glycaemic control
  - ○ Indirect bomcalorimetry
  - ○ Tissue histology and immunohistochemistry
  - ○ Quantification of adipocytes
  - ○ Flow cytometry
  - ○ Immune cell labeling with BODIPY FL C16 (palmitate) and 2-NBDG
  - ○ BMDM cell culture
  - ○ Hoxb8 cells
  - ○ In vitro ^{13}C metabolomics tracing
  - ○ In vivo ^{13}C metabolomics tracing
  - ○ Analysis of mitochondrial function
  - ○ Bone marrow transfer
  - ○ qPCR
  - ○ RNA-sequencing
- ● QUANTIFICATION AND STATISTICAL ANALYSIS

AUTHOR CONTRIBUTIONS

L.C. and B.M. performed the bulk of the experiments, analyzed the data, and wrote the manuscript. P.M. performed the Seahorse experiments. E.H. performed the bone marrow transfer experiment. C.S., A.R., and A.B. performed the flow cytometry of the liver. K.S. helped with the experiments to investigate the fat uptake in the small intestine. A.M. and M.S. performed the in vitro ^{13}C tracing experiments. B.G. performed the mass spectrometry analysis. L.M. and Y.S. analyzed the raw RNA-seq data. M.S. and H.V. provided help to L.C. during several experiments. C.M and K.R. provided tools and ideas. B.v.d.S. performed the indirect calorimetry experiments. R.K. and S.J. provided ideas and analyzed the data. G.v.L. provided ideas, analyzed the data, coordinated the project, and wrote the manuscript.

DECLARATION OF INTERESTS

The authors declare no competing interests.

REFERENCES

Arkan, M.C., Hevener, A.L., Greten, F.R., Maeda, S., Li, Z.-W., Long, J.M., Wynshaw-Boris, A., Poli, G., Olefsky, J., and Karin, M. (2005). IKK-beta links inflammation to obesity-induced insulin resistance. Nat. Med. 11, 191–198.

Bonnardel, J., T'Jonck, W., Gaublomme, D., Browaeys, R., Scott, C.L., Martens, L., Vanneste, B., De Prijck, S., Nedospasov, S.A., Kremer, A., et al. (2019). Stellate Cells, Hepatocytes, and Endothelial Cells Imprint the Kupffer Cell Identity on Monocytes Colonizing the Liver Macrophage Niche. Immunity 51, 638–654.e9.

Brestoff, J.R., and Artis, D. (2015). Immune regulation of metabolic homeostasis in health and disease. Cell 161, 146–160.

Cani, P.D., Amar, J., Iglesias, M.A., Poggi, M., Knauf, C., Bastelica, D., Neyrinck, A.M., Fava, F., Tuohy, K.M., Chabo, C., et al. (2007). Metabolic endotoxemia initiates obesity and insulin resistance. Diabetes 56, 1761–1772.

Cao, J., Perez, S., Goodwin, B., Lin, Q., Peng, H., Qadri, A., Zhou, Y., Clark, R.W., Perreault, M., Tobin, J.F., and Gimeno, R.E. (2014). Mice deleted for GPAT3 have reduced GPAT activity in white adipose tissue and altered energy and cholesterol homeostasis in diet-induced obesity. Am. J. Physiol. Endocrinol. Metab. 306, E1176–E1187.

Catrysse, L., and van Loo, G. (2017). Inflammation and the Metabolic Syndrome: The Tissue-Specific Functions of NF-κB. Trends Cell Biol. 27, 417–429.

Catrysse, L., and van Loo, G. (2018). Adipose tissue macrophages and their polarization in health and obesity. Cell. Immunol. 330, 114–119.

Catrysse, L., Vereecke, L., Beyaert, R., and van Loo, G. (2014). A20 in inflammation and autoimmunity. Trends Immunol. 35, 22–31.

Clausen, B.E., Burkhardt, C., Reith, W., Renkawitz, R., and Förster, I. (1999). Conditional gene targeting in macrophages and granulocytes using LysMcre mice. Transgenic Res. 8, 265–277.

De Wilde, K., Martens, A., Lambrecht, S., Jacques, P., Drennan, M.B., Debus-schere, K., Govindarajan, S., Coudenys, J., Verheugen, E., Windels, F., et al. (2016). A20 inhibition of STAT1 expression in myeloid cells: a novel endoge-nous regulatory mechanism preventing development of enthesitis. Ann. Rheum. Dis. *76*, 585–592.

Degrandi, D., Hoffmann, R., Beuter-Gunia, C., and Pfeffer, K. (2009). The proin-flammatory cytokine-induced IRG1 protein associates with mitochondria. J. Interferon Cytokine Res. *29*, 55–67.

Eyckerman, S., Titeca, K., Van Quickelberghe, E., Cloots, E., Verhee, A., Sa-myn, N., De Ceuninck, L., Timmerman, E., De Sutter, D., Lievens, S., et al. (2016). Trapping mammalian protein complexes in viral particles. Nat. Com-mun. *7*, 11416.

Ghesquière, B., Wong, B.W., Kuchnio, A., and Carmeliet, P. (2014). Meta-bolism of stromal and immune cells in health and disease. Nature *511*, 167–176.

Goldmann, T., Wieghofer, P., Müller, P.F., Wolf, Y., Varol, D., Yona, S., Bren-decke, S.M., Kierdorf, K., Staszewski, O., Datta, M., et al. (2013). A new type of microglia gene targeting shows TAK1 to be pivotal in CNS autoimmune inflammation. Nat. Neurosci. *16*, 1618–1626.

Gregor, M.F., and Hotamisligil, G.S. (2011). Inflammatory mechanisms in obesity. Annu. Rev. Immunol. *29*, 415–445.

Hill, D.A., Lim, H.-W., Kim, Y.H., Ho, W.Y., Foong, Y.H., Nelson, V.L., Nguyen, H.C.B., Chegireddy, K., Kim, J., Habertheuer, A., et al. (2018). Distinct macro-phage populations direct inflammatory versus physiological changes in adi-pose tissue. Proc. Natl. Acad. Sci. USA *115*, E5096–E5105.

Hotamisligil, G.S. (2006). Inflammation and metabolic disorders. Nature *444*, 860–867.

Kanda, H., Tateya, S., Tamori, Y., Kotani, K., Hiasa, K., Kitazawa, R., Kitazawa, S., Miyachi, H., Maeda, S., Egashira, K., and Kasuga, M. (2006). MCP-1 con-tributes to macrophage infiltration into adipose tissue, insulin resistance, and hepatic steatosis in obesity. J. Clin. Invest. *116*, 1494–1505.

Könner, A.C., and Brüning, J.C. (2011). Toll-like receptors: linking inflammation to metabolism. Trends Endocrinol. Metab. *22*, 16–23.

Kratz, M., Coats, B.R., Hisert, K.B., Hagman, D., Mutskov, V., Peris, E., Schoenfelt, K.Q., Kuzma, J.N., Larson, I., Billing, P.S., et al. (2014). Metabolic dysfunction drives a mechanistically distinct proinflammatory phenotype in adipose tissue macrophages. Cell Metab. *20*, 614–625.

Lumeng, C.N., and Saltiel, A.R. (2011). Inflammatory links between obesity and metabolic disease. J. Clin. Invest. *121*, 2111–2117.

Lumeng, C.N., Bodzin, J.L., and Saltiel, A.R. (2007). Obesity induces a pheno-typic switch in adipose tissue macrophage polarization. J. Clin. Invest. *117*, 175–184.

Mariathasan, S., Weiss, D.S., Newton, K., McBride, J., O'Rourke, K., Roose-Girma, M., Lee, W.P., Weinrauch, Y., Monack, D.M., and Dixit, V.M. (2006). Cryopyrin activates the inflammasome in response to toxins and ATP. Nature *440*, 228–232.

Martens, A., and van Loo, G. (2020). A20 at the Crossroads of Cell Death, Inflammation, and Autoimmunity. Cold Spring Harb. Perspect. Biol. *12*, 036418.

Matmati, M., Jacques, P., Maelfait, J., Verheugen, E., Kool, M., Sze, M., Ge-boes, L., Louagie, E., Mc Guire, C., Vereecke, L., et al. (2011). A20 (TNFAIP3) deficiency in myeloid cells triggers erosive polyarthritis resembling rheumatoid arthritis. Nat. Genet. *43*, 908–912.

Nair, S., Huynh, J.P., Lampropoulou, V., Loginicheva, E., Esaulova, E., Goun-der, A.P., Boon, A.C.M., Schwarzkopf, E.A., Bradstreet, T.R., Edelson, B.T., et al. (2018). *Irg1* expression in myeloid cells prevents immunopathology dur-ing *M. tuberculosis* infection. J. Exp. Med. *215*, 1035–1045.

Newton, K., Sun, X., and Dixit, V.M. (2004). Kinase RIP3 is dispensable for normal NF-kappa Bs, signaling by the B-cell and T-cell receptors, tumor ne-crosis factor receptor 1, and Toll-like receptors 2 and 4. Mol. Cell. Biol. *24*, 1464–1469.

O'Neill, L.A.J., and Artyomov, M.N. (2019). Itaconate: the poster child of meta-bolic reprogramming in macrophage function. Nat. Rev. Immunol. *19*, 273–281.

O'Sullivan, D., van der Windt, G.J., Huang, S.C., Curtis, J.D., Chang, C.H., Buck, M.D., Qiu, J., Smith, A.M., Lam, W.Y., DiPlato, L.M., et al. (2014). Mem-ory CD8(+) T cells use cell-intrinsic lipolysis to support the metabolic program-ming necessary for development. Immunity *41*, 75–88.

Odegaard, J.I., and Chawla, A. (2013). Pleiotropic actions of insulin resistance and inflammation in metabolic homeostasis. Science *339*, 172–177.

Ogawa, Y., Imajo, K., Honda, Y., Kessoku, T., and Tomeno, W. (2018). Palmi-tate-induced lipotoxicity is crucial for the pathogenesis of nonalcoholic fatty liver disease in cooperation with gut-derived endotoxin. Sci. Rep. *8*, 11365.

Osborn, O., and Olefsky, J.M. (2012). The cellular and signaling networks link-ing the immune system and metabolism in disease. Nat. Med. *18*, 363–374.

Pajvani, U.B., Trujillo, M.E., Combs, T.P., Iyengar, P., Jelicks, L., Roth, K.A., Kitsis, R.N., and Scherer, P.E. (2005). Fat apoptosis through targeted activa-tion of caspase 8: a new mouse model of inducible and reversible lipoatrophy. Nat. Med. *11*, 797–803.

Polykratis, A., Martens, A., Eren, R.O., Shirasaki, Y., Yamagishi, M., Yamagu-chi, Y., Uemura, S., Miura, M., Holzmann, B., Kollias, G., et al. (2019). A20 pre-vents inflammasome-dependent arthritis by inhibiting macrophage necropto-sis through its ZnF7 ubiquitin-binding domain. Nat. Cell Biol. *21*, 731–742.

Reilly, S.M., and Saltiel, A.R. (2017). Adapting to obesity with adipose tissue inflammation. Nat. Rev. Endocrinol. *13*, 633–643.

Rosen, E.D., and Spiegelman, B.M. (2014). What we talk about when we talk about fat. Cell *156*, 20–44.

Sharma, M., Schlegel, M., Brown, E.J., Sansbury, B.E., Weinstock, A., Afonso, M.S., Corr, E.M., van Solingen, C., Shanley, L.C., Peled, D., et al. (2019). Ne-trin-1 Alters Adipose Tissue Macrophage Fate and Function in Obesity. Immu-nometabolism *1*, 549–562.

Shinkai, Y., Rathbun, G., Lam, K.P., Oltz, E.M., Stewart, V., Mendelsohn, M., Charron, J., Datta, M., Young, F., Stall, A.M., et al. (1992). RAG-2-deficient mice lack mature lymphocytes owing to inability to initiate V(D)J rearrange-ment. Cell *68*, 855–867.

Silva, H.M., Báfica, A., Rodrigues-Luiz, G.F., Chi, J., Santos, P.D.A., Reis, B.S., Hoytema van Konijnenburg, D.P., Crane, A., Arifa, R.D.N., Martin, P., et al. (2019). Vasculature-associated fat macrophages readily adapt to inflamma-tory and metabolic challenges. J. Exp. Med. *216*, 786–806.

Strelko, C.L., Lu, W., Dufort, F.J., Seyfried, T.N., Chiles, T.C., Rabinowitz, J.D., and Roberts, M.F. (2011). Itaconic acid is a mammalian metabolite induced during macrophage activation. J. Am. Chem. Soc. *133*, 16386–16389.

Tanti, J.-F., Ceppo, F., Jager, J., and Berthou, F. (2013). Implication of inflam-matory signaling pathways in obesity-induced insulin resistance. Front. Endo-crinol. (Lausanne) *3*, 181.

Tian, X.Y., Ganeshan, K., Hong, C., Nguyen, K.D., Qiu, Y., Kim, J., Tangirala, R.K., Tontonoz, P., and Chawla, A. (2016). Thermoneutral Housing Accelerates Metabolic Inflammation to Potentiate Atherosclerosis but Not Insulin Resis-tance. Cell Metab. *23*, 165–178.

Tschöp, M.H., Speakman, J.R., Arch, J.R.S., Auwerx, J., Brüning, J.C., Chan, L., Eckel, R.H., Farese, R.V., Jr., Galgani, J.E., Hambly, C., et al. (2011). A guide to analysis of mouse energy metabolism. Nat. Methods *9*, 57–63.

Vande Walle, L., Van Opdenbosch, N., Jacques, P., Fossoul, A., Verheugen, E., Vogel, P., Beyaert, R., Elewaut, D., Kanneganti, T.D., van Loo, G., and Lam-kanfi, M. (2014). Negative regulation of the NLRP3 inflammasome by A20 pro-tects against arthritis. Nature *512*, 69–73.

Vereecke, L., Sze, M., Mc Guire, C., Rogiers, B., Chu, Y., Schmidt-Supprian, M., Pasparakis, M., Beyaert, R., and van Loo, G. (2010). Enterocyte-specific A20 deficiency sensitizes to tumor necrosis factor-induced toxicity and exper-imental colitis. J. Exp. Med. *207*, 1513–1523.

Vereecke, L., Beyaert, R., and van Loo, G. (2011). Genetic relationships be-tween A20/TNFAIP3, chronic inflammation and autoimmune disease. Bio-chem. Soc. Trans. *39*, 1086–1091.

Wang, G.G., Calvo, K.R., Pasillas, M.P., Sykes, D.B., Häcker, H., and Kamps, M.P. (2006). Quantitative production of macrophages or neutrophils ex vivo using conditional Hoxb8. Nat. Methods *3*, 287–293.

Weinstock, A., Brown, E.J., Garabedian, M.L., Pena, S., Sharma, M., Lafaille, J., Moore, K.J., Fisher, E.A., Behavior, S., and Neoplasms, B. (2019). Single-Cell RNA Sequencing of Visceral Adipose Tissue Leukocytes Reveals that Caloric Restriction Following Obesity Promotes the Accumulation of a Distinct Macrophage Population with Features of Phagocytic Cells. Immunometabolism *1*, e190008.

Weisberg, S.P., Hunter, D., Huber, R., Lemieux, J., Slaymaker, S., Vaddi, K., Charo, I., Leibel, R.L., and Ferrante, A.W., Jr. (2006). CCR2 modulates inflammatory and metabolic effects of high-fat feeding. J. Clin. Invest. *116*, 115–124.

Wilson, A.M., Shao, Z., Grenier, V., Mawambo, G., Daudelin, J.F., Dejda, A., Pilon, F., Popovic, N., Boulet, S., Parinot, C., et al. (2018). Neuropilin-1 expression in adipose tissue macrophages protects against obesity and metabolic syndrome. Sci. Immunol. *3*, 1–15.

Wolf, M.J., Hoos, A., Bauer, J., Boettcher, S., Knust, M., Weber, A., Simonavicius, N., Schneider, C., Lang, M., Stürzl, M., et al. (2012). Endothelial CCR2 signaling induced by colon carcinoma cells enables extravasation via the JAK2-Stat5 and p38MAPK pathway. Cancer Cell *22*, 91–105.

Xu, X., Grijalva, A., Skowronski, A., van Eijk, M., Serlie, M.J., and Ferrante, A.W., Jr. (2013). Obesity activates a program of lysosomal-dependent lipid metabolism in adipose tissue macrophages independently of classic activation. Cell Metab. *18*, 816–830.

Yu, J., Loh, K., Song, Z.Y., Yang, H.Q., Zhang, Y., and Lin, S. (2018). Update on glycerol-3-phosphate acyltransferases: the roles in the development of insulin resistance. Nutr. Diabetes *8*, 34.

Zhang, C., Cooper, D.E., Grevengoed, T.J., Li, L.O., Klett, E.L., Eaton, J.M., Harris, T.E., and Coleman, R.A. (2014). Glycerol-3-phosphate acyltransferase-4-deficient mice are protected from diet-induced insulin resistance by the enhanced association of mTOR and rictor. Am. J. Physiol. Endocrinol. Metab. *307*, E305–E315.

KEY RESOURCES TABLE

REAGENT or RESOURCE	SOURCE	IDENTIFIER
Antibodies		
UCP1	Abcam	Cat# ab10983; RRID:AB_2241462
CD206-Biotin coupled	Bio-Rad	Cat# MCA2235BT; RRID:AB_1101315
CD11c-eFluor660	eBioscience	Cat# 50-0114-80; RRID:AB_11151322
Ly6C-eFluor450	eBioscience	Cat# 48-5932-82; RRID:AB_10805519
CD45-BV510	BioLegend	Cat# 103137; RRID:AB_2561392
CD64-BV711	Biolegend	Cat# 139311; RRID:AB_2563846
F4/80-Biotin	eBioscience	Cat# 13-4801-81; RRID:AB_466656
Streptavidin- BV786	BD	Cat# 563858; RRID:AB_2869529
CD206-APC	Biolegend	Cat# 141707; RRID:AB_10896057
Fixable live dead dye eFluor780	eBioscience	Cat# 65-0865
Siglec F-PE	BD	Cat# 552126; RRID:AB_394341
CD11c-PE-Texas Red	Invitrogen	Cat# MCD11C17; RRID:AB_10373971
Gr1-PE Cy5	eBioscience	Cat# 15-5931-81; RRID:AB_468812
CD11b-PE Cy7	BD	Cat# 552850; RRID:AB_394491
anti-rabbit-HRP	Dako	Cat# P0448; RRID:AB_2617138
CD11c-PE-eFluor610	eBioscience	Cat# 61-0114-82; RRID:AB_2574530
Ly-6G-PE	BD	Cat# 551461; RRID:AB_394208
Siglec F-PE	BD	Cat# 552126; RRID:AB_394341
Ly-6C-eFluor450	eBioscience	Cat# 48-5932-82; RRID:AB_10805519
Streptavidin-BV605	BD	Cat# 563260; RRID:AB_2869476
F4/80e-eFluor450	eBioscience	Cat# 48-4801-82; RRID:AB_1548747
B220-APC	eBioscience	Cat# 17-0452-81; RRID:AB_469394
CD45-PE	eBioscience	Cat# 12-0451-82; RRID:AB_465668
CD3-PE Cy7	Biolegend	Cat# 100219; RRID:AB_1732068
Fixable Viability Dye eFluor506	Life Technologies	Cat# 65-0866-18
Ly-6G BD Optibuild BV650	BD Biosciences	Cat# 740554; RRID:AB_2740255
F4/80 BV786	BioLegend	Cat# 123141; RRID:AB_2563667
CD206 APC	BioLegend	Cat# 141708; RRID:AB_10900231
CD45 AlexaFluor 700	Life Technologies	Cat# 56-0451-82; RRID:AB_891454
MHCII APC-eFluor780	eBioscience	Cat# 47-5321-82; RRID:AB_1548783
Lyve-1 biotin	eBioscience	Cat# 13-0443-82; RRID:AB_1724157
streptavidin PE-CF594	BD Biosciences	Cat# 562284; RRID:AB_11154598
CD3e PE-Cy5	eBioscience	Cat# 15-0042-83; RRID:AB_468699
CD19 PE-Cy5	eBioscience	Cat# 15-0193-83; RRID:AB_657673
CD11c PE-Cy7	eBioscience	Cat# 25-0114-82; RRID:AB_469590
CD11b BUV395	BD Biosciences	Cat# 563553; RRID:AB_2738276
CD45-FITC	eBioscience	Cat# 11-0451-82; RRID:AB_465050
Ly6C-PE	BD	Cat# 560592; RRID:AB_1727556
CD11b-BV421	BD	Cat# 562605; RRID:AB_11152949
CD206-APC	Biolegend	Cat# 141707; RRID:AB_10896057
Chemicals, peptides, and recombinant proteins		
TRIzol reagent	Thermo Fisher Scientific	cat# 15596026
collagenase type II	Sigma	cat# 1764

(Continued on next page)

Continued

REAGENT or RESOURCE	SOURCE	IDENTIFIER
ACK lysis buffer	Thermo Fisher Scientific	cat# A1049201
DNase	Roche	cat# 04 536 282 001
Brewer thioglycollate medium	Sigma	cat# B-2551
L-glutamin	Lonza	cat# BE17-605F
RPMI 1640	Caisson Labs	cat# RPP24-1LT
Sodium pyruvate	Sigma-Aldrich	cat# S-8636
Penicillin-Streptomycin	GIBCO	cat#15140-122
fetal calf serum	Bodinco	n/a
LPS (*E. coli* 0111:B4 strain)	InvivoGen	n/a
IFNy	Produced in house	n/a
Ficoll Paque Plus	Sigma	cat# GE17-1440-02
BODIPY FL C16	Thermo Fisher Scientific	cat# D-3821
GM-CSF	Produced in house	n/a
2-NBDG	Thermo Fisher Scientific	cat# N13195
BD Horizon Brilliant Stain Buffer	BD Biosciences	cat# 566349
recombinant mouse M-CSF	Produced in house	n/a
Estradiol	Sigma	cat# E8875
Fibronectin	Sigma	n/a
Polybrene	Sigma	cat# TR-1003
G418	ThermoFisher Scientific	cat# 10131035
Glycerol	Biosolve	cat# 7122301
Lecithin	Wako chemicals	cat# 120-00832
13C labeled ethyl ester palmitic acid	Cambridge Isotope Laboratories	cat# CLM-3957-0
Liberase TM	Roche	cat# 5401119001
Critical commercial assays		
Aurum Total RNA Isolation Mini Kit	BioRad	cat# 7326820
iScript cDNA synthesis kit	Bio-Rad Laboratories	cat# 1708890
SensiFAST SYBR® No-ROX Kit	GeC Biotech	cat# CSA-01190
RNeasy Plus Micro Kit	QIAGEN	cat# 74034
XFe96 cell culture plates	Agilent technologies	cat# 101085-004
Seahorse XF Long Chain Fatty Acid Oxidation Stress Test Kit	Agilent technologies	cat# 103672-100
Bioplex mouse TNF assay	Biorad	cat# 171G5023M
Bioplex mouse IL6 assay	Biorad	cat# 171G5007M
Bioplex mouse MCP1 assay	Biorad	cat# 171G5019M
Bioplex mouse RANTES assay	Biorad	cat# 171G5022M
Mouse IL-18 ELISA kit	MBL	cat# 7625
Free Fatty Acid Assay Kit	Abnova	cat# KA1667
RayBio® Mouse Leptin ELISA kit	RayBio Inc	cat# ELM-Leptin-1
Triglyceride Colorimetric Assay Kit	Cayman Chemical	cat# 10010303
Ultra Sensitive Mouse Insulin ELISA kit	Crystal Chem	cat# 90080
Agilent RNA 600 Nano kit	Agilent Technologies	n/a
SMART-Seq V4 Ultra Low Input kit	Takara	cat# 634888
NEBNext Ultra DNA Library Prep kit	New England Biolabs	cat# E7370S
Deposited data		
RNaseq data	this paper	GEO: GSE182155
Experimental models: Cell lines		
mouse: primary macrophages (BMDM and peritoneal)	this paper	n/a

Continued

REAGENT or RESOURCE	SOURCE	IDENTIFIER
Hoxb8	this paper	n/a
Experimental models: Organisms/strains		
mouse: A20^{FL}	Vereecke et al., 2010	n/a
mouse: LysM Cre	Clausen et al., 1999	n/a
mouse: Cx3Cr1ERT2 Cre	Goldmann et al., 2013	n/a
mouse: Irg1^{FL}	Nair et al., 2018	n/a
mouse: Nlrp3$^{-/-}$	Mariathasan et al., 2006	n/a
mouse: Ripk3$^{-/-}$	Newton et al., 2004	n/a
mouse: Rag2$^{-/-}$	Shinkai et al., 1992	n/a
mouse: Ccr2^{FL}	Wolf et al., 2012	n/a
Oligonucleotides		
qPCR primers	see Table S1	n/a
Software and algorithms		
ZEN (blue edition)	Zeiss	https://www.zeiss.com/microscopy/int/products/microscope-software/zen.html
FlowJo.10	n/a	https://www.flowjo.com/
GraphPad Prism 8	n/a	https://www.graphpad.com/
Fluostar Omega	BMG Labtech	https://www.bmglabtech.com/fluostar-omega/
XCalibur version 4.2.28.14	Thermo Scientific	n/a
MSigDB	n/a	https://www.gsea-msigdb.org/gsea/msigdb
Genstat v19	VSN International	n/a
Other		
Axioscan Z1	Zeiss	n/a
LSR Fortessa 4 laser cytometer	BD Biosciences	n/a
LightCycler 480 II	Roche	n/a
TissueLyser II	QIAGEN	n/a
Vanquish LC System	Thermo Scientific	n/a
Hilicon iHILIC-Fusion(P) SS column SS	Achrom	n/a
Lumos Orbitrap mass spectrometer	Thermo Scientific	n/a
glucometer (Freestyle Lite)	Abbott	n/a
paramagnetic oxygen analyzer	Servomex Xentra 4100	n/a
infrared gas analyzer	Servomex 1440	n/a
mass-flow controller (Type 5850)	Brooks	n/a
passive infrared detectors	Optex Wonderex FX-35	n/a
light microscope	Olympus BX51	n/a
confocal fluorescent microscope	Zeiss	n/a
Cryostat	Microm HM560	n/a
Nanodrop	Thermo Fisher Scientific	n/a

RESOURCE AVAILABILITY

Lead contact
Further information and requests for resources and reagents may be directed to Geert van Loo (Lead contact; geert.vanloo@irc.vib-ugent.be).

Materials availability
Resources and reagents generated in this study are available from the Lead Contact but may require a Materials Transfer Agreement to be signed.

Data and code availability

- All data and code supporting the findings of this study are available within the paper or are available from the lead contact upon request.
- RNA-seq data have been deposited at Gene Expression Omnibus (GEO) and are publicly available with accession number GEO: GSE182155.
- Any additional information required to reanalyze the data reported in this work paper is available from the Lead Contact upon request.

EXPERIMENTAL MODEL AND SUBJECT DETAILS

Animals

Mice with conditional loxP-flanked A20 (Vereecke et al., 2010) were crossed with LysM-Cre transgenic mice (Clausen et al., 1999) to generate a myeloid-specific A20 knockout mouse (A20$^{myel-KO}$ mice), as previously described (Matmati et al., 2011). Alternatively, A20$^{FL/FL}$ mice were crossed with Cx3Cr1ERT2Cre transgenic mice (Goldmann et al., 2013) and A20 deletion was induced by injecting mice subcutaneously at 4 places with 50 μl of Tamoxifen dissolved in corn oil (20 mg/ml) twice a week to induce continuous deletion of A20 in myeloid cells. A20$^{myel-KO}$ mice were crossed with Irg1$^{FL/FL}$ (Nair et al., 2018), CCR2$^{FL/FL}$ (Wolf et al., 2012), NLRP3$^{-/-}$ (Mariathasan et al., 2006), RIPK3$^{-/-}$ (Newton et al., 2004) or Rag2$^{-/-}$ (Shinkai et al., 1992) mice to generate A20-Irg1$^{myel-DKO}$, A20-CCR2$^{myel-DKO}$, A20$^{myel-KO}$NLRP3$^{-/-}$, A20$^{myel-KO}$RIPK3$^{-/-}$ or A20$^{myel-KO}$Rag2$^{-/-}$ mice, respectively. A20$^{myel-KO}$ mice were treated by intraperitoneal injection every 4 days with neutralizing anti-TNF antibodies (MP6-XT22 mAb, 20 mg/kg body weight), anti-IL-6 antibodies (20F3 mAb, 10 mg/kg body weight), and isotype control antibodies, as previously described (Matmati et al., 2011). All experiments were performed on mice backcrossed into the C57BL/6J genetic background for at least ten generations. Mice were housed in individually ventilated cages in a specific pathogen-free animal facility of the VIB Center for Inflammation Research. Male littermate mice were fed with either a standard diet (10% kcal fat, Research Diets Inc, D12450B) or a high fat diet (60% kcal fat, Research Diets Inc, D12492) from the age of 8 weeks on. All experiments on mice were performed according to institutional, national and European animal regulations.

Cells

Bone Marrow Derived Macrophages (BMDMs) were obtained from bone marrow cells flushed from mouse femurs and tibia, and cultured in RPMI 1640 supplemented with 40 ng/ml recombinant mouse M-CSF, 10% FCS, 1% penicillin/streptavidin and glutamine. Fresh M-CSF was added on day 3 and medium was refreshed on day 5. On day 7 cells were seeded and stimulated. Peritoneal macrophages were isolated by injecting mice intra-peritoneally with 3 mL of Brewer thioglycollate medium (Sigma, B-2551) 4 days before sacrifice. 5 mL of PBS with 5 mM EDTA was injected intra-peritoneally with a small needle, the abdomen was gently massaged and most of the liquid was again retracted using a larger needle. The cells were spun down at 300 g for 3 min, the supernatans was removed and the cells were counted and cultured overnight in RPMI, 10% FCS, 1% penicillin/streptavidin, glutamine and sodium pyruvate. Immortalized macrophage Hoxb8 cells were generated as described previously (Wang et al., 2006). In short, bone marrow cells were collected from femur and tibia of 8 week old mice by flushing with RPMI (ThermoFisher Scientific). Progenitor cells were purified by centrifugation over 3 mL Ficoll Paque Plus (Sigma), and resuspended in progenitor outgrowth medium (POM) consisting of RPMI (ThermoFisher Scientific) supplemented with 10% FCS (Bodinco), 1% penicillin/streptomycin (ThermoFisher Scientific), 20 ng/ml GM-CSF (produced by the VIB Protein Core Facility) and 1 μM β-estradiol (Sigma). 250.000 cells per well were plated in 1 mL of POM in a fibronectin (Sigma) coated 12-well plate. Cells were infected by spinoculation (1000 g for 1 h) with Hoxb8-ER retroviral particles and in presence of 0.8 ug/ml polybrene (Sigma). 3 mL of POM was added after spinfection. After 24 h hours, cells were collected, pelleted by centrifugation and seeded in POM containing 1 μg/ml G418 (ThermoFisher Scientific) in 12-well suspension plates. Cells were split every 3-4 days until cell populations were stably expanding. For differentiation to macrophages, cells were washed twice with PBS to remove residual β-estradiol and plated at 10^6 cells per 10 cm bacterial plate in 10 mL complete medium containing 50 ng/ml M-CSF. On day 3, 10 mL fresh medium was added, on day 5 medium was completely refreshed, and on day 6 cells were seeded in TC-coated plates.

METHOD DETAILS

Animals

Mice with conditional loxP-flanked A20 (Vereecke et al., 2010) were crossed with LysM-Cre transgenic mice (Clausen et al., 1999) to generate a myeloid-specific A20 knockout mouse (A20$^{myel-KO}$ mice), as previously described (Matmati et al., 2011). Alternatively, A20$^{FL/FL}$ mice were crossed with Cx3Cr1ERT2Cre transgenic mice (Goldmann et al., 2013) and A20 deletion was induced by injecting mice subcutaneously at 4 places with 50 μl of Tamoxifen dissolved in corn oil (20 mg/ml) twice a week to induce continuous deletion of A20 in myeloid cells. A20$^{myel-KO}$ mice were crossed with Irg1$^{FL/FL}$ (Nair et al., 2018), CCR2$^{FL/FL}$ (Wolf et al., 2012), NLRP3$^{-/-}$ (Mariathasan et al., 2006), RIPK3$^{-/-}$ (Newton et al., 2004) or Rag2$^{-/-}$ (Shinkai et al., 1992) mice to generate A20-Irg1$^{myel-DKO}$,

A20-CCR2$^{myel-DKO}$, A20$^{myel-KO}$NLRP3$^{-/-}$, A20$^{myel-KO}$RIPK3$^{-/-}$ or A20$^{myel-KO}$Rag2$^{-/-}$ mice, respectively. A20$^{myel-KO}$ mice were treated by intraperitoneal injection every 4 days with neutralizing anti-TNF antibodies (MP6-XT22 mAb, 20 mg/kg body weight), anti-IL-6 antibodies (20F3 mAb, 10 mg/kg body weight), and isotype control antibodies, as previously described (Matmati et al., 2011). All experiments were performed on mice backcrossed into the C57BL/6J genetic background for at least ten generations. Mice were housed in individually ventilated cages in a specific pathogen-free animal facility of the VIB Center for Inflammation Research. Mice were fed with either a standard diet (10% kcal fat, Research Diets Inc, D12450B) or a high fat diet (60% kcal fat, Research Diets Inc, D12492) from the age of 8 weeks on. All experiments on mice were performed according to institutional, national and European animal regulations.

DEXA scan
DEXA scanning was used to measure percentage of total body fat, lean mass and fat mass. These measurements were performed as described (Pajvani et al., 2005).

Analytical assays
Cytokines (TNF, MCP-1, IL-6, RANTES) were measured in the serum of the mice using the Bioplex®Multiplex Immunoassay System (Biorad). IL-18 levels were determined using the Mouse IL-18 ELISA kit (MBL, 7625). Free fatty acid levels were determined using the Free Fatty Acid Assay Kit (Abnova, KA1667) and leptin levels were determined using the RayBio® Mouse Leptin ELISA kit (RayBio Inc). All assays were performed according to the manufacturer's instructions. Triglyceride and cholesterol levels were determined from serum in the Laboratory of Clinical Biology of the University Hospital Ghent, according to standard procedures. Triglyceride levels in liver was determined using the Triglyceride Colorimetric Assay Kit (Cayman Chemical, 10010303). Itaconic acid levels were determined using the Lumos Orbitrap mass spectrometer (Thermo Scientific) and LC-Q-Exactive.

Assessment of glycaemic control
For the intraperitoneal glucose tolerance test (ipGTT), mice were injected with 2 g/kg glucose after an overnight fast. Tail blood samples were collected at indicated time points after injection, and glucose levels were determined using a glucometer (Freestyle Lite, Abbott). Serum insulin levels were determined by the Ultra Sensitive Mouse Insulin ELISA kit (Crystal Chem, 90080). For the insulin tolerance test (ITT), mice were injected with 0.75 U of insulin/g body weight after a 4 hour starvation period, and glucose levels were determined from tail blood by using a glucometer.

Indirect bomcalorimetry
Animals were housed individually in metabolic cages for 4 to 7 days. Oxygen and carbon dioxide concentration of dried inlet and outlet air from each chamber were measured with a paramagnetic oxygen analyzer (Servomex Xentra 4100) and carbon dioxide by an infrared gas analyzer (Servomex 1440). Flow rate of inlet air (60 l/hour) was measured with a mass-flow controller (Type 5850 Brooks). Ambient temperature in the room and chambers, as well as behavioral activity were measured simultaneously with passive infrared detectors (Optex Wonderex FX-35). Measurements were collected every 10 minutes (allowing optimal air mixing) for each animal and automatically stored on a computer. To reduce novel cage stress, the respirometric chambers (45x25x30 cm) were adapted to accommodate the home cage of the animal. Animals were measured at an ambient temperature of 22°C and food and water were provided *ad libitum*. Food intake was measured by manually weighing the food provided to the individual mice.

Tissue histology and immunohistochemistry
Histology was performed on paraffin-embedded (5 μm) tissue sections. Briefly, tissues were dissected and fixed in 4% paraformaldehyde and embedded in paraffin. Hematoxylin and eosin staining was performed according to a standard protocol using the Varistain (Thermo Fisher Scientific). For UCP1 staining, a UCP1-specific antibody (Abcam, ab10983) was used at a dilution of 1:500 followed by staining with Envision anti-Rabbit HRP (Dako). Images were taken with an Olympus BX51 light microscope. For immunofluorescence microscopy, whole mount adipose tissue was used, and adipose tissue (5 mm^2) was left to dry on a slide coated with CellTAK (Corning) and stained with anti-CD206-Biotin coupled (AbD Serotec, MCA2235BT) and anti-CD11c-eFluor660 (eBioscience, 50-0114) for 24 hours, after which the slides were mounted and imaged using a confocal fluorescent microscope (Zeiss). For the Oil Red O staining, the small intestine was isolated, fixed in 4% paraformaldehyde for one hour, left overnight in 30% sucrose in PBS, prepared for freeze sections in Mec-60 and cut at 10 micron on a cryostat (Microm HM560). The slides were washed with PBS, washed with absolute propylene glycol for 5 minutes, stained with pre-warmed 0.5% Oil Red O dissolved in propylene glycol at 60 degrees for 10 minutes, destained with 85% propylene glycol for 5 minutes, washed under running tap water, counterstained with hematoxylin, mounted and imaged with an Olympus BX51 light microscope.

Quantification of adipocytes
5 μm sections from a complete eWAT fat pad were stained with hematoxylin and eosin and imaged using the slide scanner AxioScan Z1 (Zeiss), allowing visualization of the entire fat pad. Number and size of adipocytes were quantified using Fiji software.

Flow cytometry

Epididymal fat pads were isolated from mice, weighed and put in cold PBS + 0.5% BSA. Briefly, the fad pad was cut into pieces and digested in DMEM + 0.5% BSA + 10 mM $CaCl_2$ supplemented with 2 mg/ml collagenase type II (Sigma, 1764) at 37°C until single cell suspension. After collagenase neutralization with cold PBS + 0.5% BSA, the suspension was filtered through a 100 μm filter, washed and treated with ACK lysis buffer (Thermo Fisher Scientific). Cells were resuspended in FACS buffer (PBS, 0.5% BSA, 2 mM EDTA), counted and diluted to a concentration of 10 million cells/ml. Cells were stained with the following antibodies: Ly6C-eFluor450 (eBioscience, 48-5932-82), CD45-BV510 (BioLegend, 103137), CD64-BV711 (Biolegend, 139311), F4/80-Biotin (eBioscience, 13-4801), Streptavidin- BV786 (BD, 563858), CD206-APC (Biolegend, 141707), Fixable live dead dye eFluor780 (eBioscience, 65-0865), Siglec F-PE (BD, 552126), CD11c-PE-Texas Red (Invitrogen, MCD11C17), Gr1-PE Cy5 (eBioscience, 15-5931), CD11b-PE Cy7 (BD, 552850). After filtration through a 30 μm filter, cells were analyzed on the LSR Fortessa 4 laser cytometer (BD). CountBright beads (Molecular probes) were used for the quantification of cells and normalized to the weight of the analyzed eWAT. For the isolation of liver leukocytes, livers were isolated from PBS-perfused mice, chopped finely and subjected to GentleMACS dissociation and incubated for 20 min with 1 mg/ml Collagenase A (Sigma) and 10U/ml DNase (Roche) in a shaking water bath at 37°C. Following a second round of GentleMACS dissociation, single cell suspensions were filtered over a 100 μm filter. Cells were resuspended in FACS buffer and stained with the following antibodies: Fixable live dead dye eFluor780 (eBioscience, 65-0865), CD11c-PE-eFluor610 (eBioscience, 61-0114-82), Ly-6G-PE (BD, 551461), Siglec F-PE (BD, 552126), Ly-6C-eFluor450 (eBioscience, 48-5932-82), CD11b-PE-Cy7 (BD, 552850), F4/80-Biotin (eBioscience, 13-4801-85), Streptavidin-BV605 (BD, Horizon 563260) and CD64-BV711 (Biolegend, 139311). For the peritoneal fluid, 200 μl of fluid was centrifuged for 3 min at 300 x g and stained with the following antibodies: F4/80e-eFluor450 (eBioscience, 48-4801-82), CD64-BV711 (Biolegend, 139311), B220-APC (eBioscience, 17-0452-81), Fixable live dead dye eFluor780 (eBioscience, 65-0865), CD45-PE (eBioscience, 12-0451), CD3-PE Cy7 (Biolegend, 100219). After filtration through a 30 μm filter, cells were analyzed on the LSR Fortessa 4 laser cytometer (BD).

Immune cell labeling with BODIPY FL C16 (palmitate) and 2-NBDG

Mice were kept on standard or high fat diet as described before. Epididymal fat pads were isolated from mice, weighed and put in cold PBS + 0.5% BSA and processed as described earlier. Spleen was isolated and kept on ice cold RPMI 1640 (Thermo Fisher Scientific) until processing. Next, spleens were smashed over a 70 μm mesh filter, washed and after centrifugation treated with ACK lysis buffer (Thermo Fisher Scientific) to remove red blood cells. Liver cells were isolated by liver perfusion and digestion as described previously (Bonnardel et al., 2019). Briefly, after retrograde cannulation, livers were perfused for 1-2 mins with an EGTA-containing solution, followed by a 5 min (6 ml/min) perfusion with 0.2 mg/mL collagenase A. Livers were then removed, minced and incubated for 20 min with 0.4 mg/mL collagenase A and 10 U/mL DNase at 37°C. All subsequent procedures were performed at 4°C. Samples were filtered over a 100 μm mesh filter and red blood cells were lysed. Samples were again filtered over a 40 μm mesh filter. After two centrifugation steps of 1 min at 50 g to remove hepatocytes, remaining liver cells (leukocytes, LSECs and HSCs) were centrifuged at 400 g for 5 min. Next, eWAT, spleen and liver immune cells were resuspended in PBS, counted and 0.5-1 × 10^6 cells were seeded in a 96-well plate. Cells were incubated with 2-NBDG (100 μM; Thermo Fisher Scientific, N13195) diluted in RPMI 1640 supplemented with 2 mM L-glutamine, 100 U/ml penicillin/streptomycin and 55 μM β-mercaptoethanol for 10 min at 37°C. For assaying BODIPY FL C16 (Thermo Fisher Scientific, D-3821) uptake, cells were incubated with the reagent (1 μM) diluted in RPMI 1640 (Thermo Fisher Scientific) supplemented with 10% fetal calf serum, 2 mM L-glutamine, 100 U/ml penicillin/streptomycin and 55 μM β-mercaptoethanol for 30 min at 37°C. Uptake was stopped by adding ice cold PBS, after which cells were washed before proceeding to staining with fluorescent labeled antibodies. To allow broad immunophenotyping of substrate labeled immune cells, cells were stained with following antibodies/reagents diluted in BD Horizon Brilliant Stain Buffer (BD Biosciences, 566349): Ly-6C-eFluor450 (eBioscience, 48-5932-82), Fixable Viability Dye eFluor506 (Life Technologies, 65-0866-18), Ly-6G BD Optibuild BV650 (BD Biosciences, 740554), CD64 BV711 (BioLegend, 139311), F4/80 BV786 (BioLegend, 123141), CD206 APC (BioLegend, 141708), CD45 AlexaFluor 700 (Life Technologies, 56-0451-82), MHCII APC-eFluor780 (eBioscience, 47-5321-82), Siglec-F PE (BD Biosciences, 552126), Lyve-1 biotin (eBioscience, 13-0443-82), streptavidin PE-CF594 (BD Biosciences, 562284), CD3e PE-Cy5 (eBioscience, 15-0042-83), CD19 PE-Cy5 (eBioscience, 15-0193-83), CD11c PE-Cy7 (eBiosciences, 25-0114-82), CD11b BUV395 (BD Biosciences, 563553). After filtration through a 40 μm filter, cells were analyzed on the LSR Fortessa 5 laser cytometer (BD).

BMDM cell culture

Bone Marrow Derived Macrophages (BMDMs) were obtained from bone marrow cells flushed from mouse femurs and tibia with ice-cold sterile RPMI medium, and cultured in RPMI 1640 supplemented with 40 ng/ml recombinant mouse M-CSF, 10% FCS, 1% penicillin/streptavidin and glutamine. Fresh M-CSF was added on day 3 and medium was refreshed on day 5. On day 7 cells were seeded and stimulated. Peritoneal macrophages were isolated by injecting mice intra-peritoneally with 3 mL of Brewer thioglycollate medium (Sigma, B-2551) 4 days before sacrifice. 5 mL of PBS with 5 mM EDTA was injected intra-peritoneally with a small needle, the abdomen was gently massaged and most of the liquid was again retracted using a larger needle. The cells were spun down at 300 g for 3 min, the supernatans was removed and the cells were counted and cultured overnight in RPMI, 10% FCS, 1% penicillin/streptavidin, glutamine and sodium pyruvate. After washing, the cells were stimulated for 16 h with 100 ng/ml LPS (*E. coli* 0111:B4 strain, InvivoGen) and 100 ng/ml IFNγ (produced by the VIB Protein Core Facility) and RNA was isolated.

Hoxb8 cells

Immortalized macrophage progenitors were generated as described previously (Wang et al., 2006). Bone marrow cells were collected from femur and tibia of 8 week old mice by flushing with RPMI (ThermoFisher Scientific). Progenitor cells were purified by centrifugation over 3 mL Ficoll Paque Plus (Sigma). Cells were resuspended in progenitor outgrowth medium (POM) consisting of RPMI (ThermoFisher Scientific) supplemented with 10% FCS (Bodinco), 1% penicillin/streptomycin (ThermoFisher Scientific), 20 ng/ml GM-CSF (produced by the VIB Protein Core Facility) and 1 μM β-estradiol (Sigma). 250.000 cells per well were plated in 1 mL of POM in a fibronectin (Sigma) coated 12-well plate. Cells were infected by spinoculation (1000 g for 1 h) with Hoxb8-ER retro-viral particles and in presence of 0.8 ug/ml polybrene (Sigma). 3 mL of POM was added after spinfection. After 24 h hours, cells were collected, pelleted by centrifugation and seeded in POM containing 1 μg/ml G418 (ThermoFisher Scientific) in 12-well suspension plates. Cells were split every 3-4 days until cell populations were stably expanding. For differentiation to macrophages, cells were washed twice with PBS to remove residual β-estradiol and plated at 10^6 cells per 10 cm bacterial plate in 10 mL complete medium containing 50 ng/ml M-CSF. On day 3, 10 mL fresh medium was added, on day 5 medium was completely refreshed, and on day 6 cells were seeded in TC-coated plates.

In vitro ^{13}C metabolomics tracing

On day 7 BMDMs were seeded and stimulated with 10 ng/ml ultrapure LPS (*E. coli* 0111:B4 strain, InvivoGen) and 10 ng/ml IFNγ (Protein Core Facility) dissolved in RPMI 1640 (Caisson Labs, #RPP24-1LT) supplemented with 1% penicillin/streptavidin. The three tracing metabolites glucose (550 mM), glutamine (200 mM) and palmitic acid (150 mM) conjugated to BSA were added in equal amounts in either ^{12}C or ^{13}C form, depending on the condition. After two days, the cells were washed with cold 0.9% NaCl solution and the metabolites were extracted using an 80% methanol (in water) extraction buffer containing 2 μM of deuterated (d27) myristic acid as internal standard, spun down at 20 000 g for 10 min at 4 degrees, after which the supernatant was analyzed on a Vanquish LC System (Thermo Scientific) in-line connected to a Lumos Orbitrap mass spectrometer (Thermo Scientific). 5 μl of the sample was injected and concentrated on a Hilicon iHILIC-Fusion(P) SS precolumn after which it was loaded onto a Hilicon iHILIC-Fusion(P) SS column SS (Achrom). A linear gradient was carried out starting with 90% solvent A (LC-MS grade acetonitrile) and 10% solvent B (10 mM ammoniumacetate pH 9.3). From 2 to 20 minutes the gradient changed to 80% B and was kept at 80% until 23 min. Next a decrease to 40% B was carried out to 25 min, further decreasing to 10% B at 27 min. Finally 10% B was maintained until 35 min. The solvent was used at a flow rate of 200 ul/min, the columns temperature was kept constant at 25°C. The mass spectrometer operated in negative ion mode, settings of the HESI probe were as follows: sheath gas flow rate at 35, auxiliary gas flow rate at 14. Spray voltage was set at 2.9 kV, temperature of the capillary at 300°C and S-lens RF level at 50. A full scan (resolution of 240.000 and scan range of m/z 70-750) was applied. For the data analysis we used XCalibur version 4.2.28.14 (Thermo Scientific).

In vivo ^{13}C metabolomics tracing

Mice were injected intra-peritoneally with 3 mL of Brewer thioglycollate medium (Sigma, B-2551) 4 days before sacrifice. The *in vivo* labeling strategy was based on Ogawa et al. (2018). The control solution was made by warming glycerol (Biosolve, 7122301) and adding lecithin (Wako chemicals, 120-00832) dropwise under heat, after which water was added dropwise under low heat to get a stock solution of 10% glycerol and 4,8% lecithin. ^{13}C labeled ethyl ester palmitic acid (Cambridge Isotope Laboratories, CLM-3957-0) was dissolved in this stock solution and further diluted with water to a concentration of 30 mM palmitic acid, 1.2% lecithin and 2.5% glycerol and sonicated to fully emulsify the ethyl ester palmitic acid. For the control solution the stock solution was further diluted with water to a concentration of 1.2% lecithin and 2.5% glycerol. The mice were injected with 3 μmol ^{13}C palmitate or the control solution intra-peritoneally, and after 4 hours the intraperitoneal fluid was isolated. In short, 5 mL of PBS with 5 mM EDTA was injected intra-peritoneally with a small needle, the abdomen was gently massaged and most of the liquid was again retracted using a larger needle. The cells were spun down at 300 g for 3 min, the supernatans was removed and the pellet was dissolved in 250 ul of the aforementioned extraction buffer, spun down at 20 000 g for 10 min at 4 degrees, after which the supernatans (5 uL) was analyzed on the LC-OrbiTRAP Lumos Fusion.

Analysis of mitochondrial function

Wild-type and A20 knockout HoxB8 cells or BMDMs were seeded in XFe96 cell culture plates (Agilent technologies) at a density of 500.000 cells/well in a XFe96 cell culture microplate a day before the experiment. OCR values were obtained from running mitochondrial stress tests according to the manufacturer's instructions. During the assay, the sequential injections were done at the following concentrations: oligomycin -1.5 μM, FCCP- 1.5 μM and rotenone/AntimycinA- 0.5 μM. In order to gauge the utilization of intrinsic fatty acid by wild-type and A20 knockout HoxB8 derived macrophages we performed the Seahorse XF Long Chain Fatty Acid Oxidation Stress Test Kit according to the manufacturers instructions. The drugs were used at the following concentrations for sequential injections- Etomoxir at 4 μM, oligomycin -1.5 μM, FCCP- 1.5 μM and rotenone/AntimycinA- 0.5 μM.

Bone marrow transfer

Allogenic bone marrow transplants were performed 24 h after myeloablative total body irradiation

(8 Gy) of recipient male mice (age ranging from 7-12 weeks). Donor bone marrow was isolated from the tibia and femur of female A20$^{FL/FL}$LysM CreTg/+CCR2eGFP$^{FL/+}$ and A20$^{FL/FL}$LysM Cre+/+CCR2eGFP$^{FL/+}$ mice. Bone marrow reconstitution was performed

by intravenous injection of 5 × 10^6 bone marrow-derived cells in 200 mL of PBS 24 h after irradiation. After a recovery phase of 6 weeks, mice were fed with High Fat Diet as previously described.

qPCR

Tissues were harvested from mice and immediately frozen in liquid nitrogen. Tissues or cells were homogenized in TRIzol® (Thermo Fisher Scientific) using the TissueLyser II (QIAGEN). Chloroform was added (1:10) and after prolonged vortexing samples were centrifuged at 13 000 rpm. The upper phase was mixed with an equal volume of 70% ethanol, followed by RNA isolation according to manufacturer's instructions using the Aurum total RNA mini kit (Bio-rad Laboratories). cDNA synthesis was performed using the iScript cDNA synthesis kit (Bio-Rad Laboratories) and 10 ng of cDNA was used for quantitative PCR in a total volume of 5 µl SensiFastSYBR No-ROX (Bioline) on the LightCycler 480 (Roche). Real-time PCR reactions were performed in triplicate using mouse-specific primers. Sequences of the mouse-specific primers are summarized in Table S1.

RNA-sequencing

Epididymal fat pads were digested in DMEM + 2% BSA supplemented with 0.28 U/ml Liberase TM (Roche) and 100 U/ml DNase I (Roche) at 37°C until single cell suspension. Cells were stained with the following antibodies: CD45-FITC (eBioscience, 11-0451), Siglec F-PE (BD, 552126), Ly6G-PE (BD, 551461), Ly6C-PE (BD, 560592), CD11c-PE-Cy7 (eBioscience, 250114), CD11b-BV421 (BD, 562605), CD64-BV711 (Biolegend, 139311), CD206-APC (Biolegend, 141707), F4/80-Biotin (eBioscience, 13-4801), Streptavidin-eFluor710 (BD, 563858), Fixable live dead stain eFluor780 (eBioscience, 65-0865). After filtration through a 30 µm filter the cells were sorted using the FACS ARIA III (BD) directly in RLT plus lysis buffer supplemented with β-mercaptoethanol and RNA was isolated using the RNeasy Plus Micro Kit (QIAGEN) according to the manufacturer's protocol. RNA quality was checked using the Nanodrop (Thermo Fisher Scientific) and the Agilent RNA 600 Nano kit (Agilent Technologies). Only samples with a RIN value above 8 were used. RNA samples were transcribed into cDNA and amplified using a SMART-Seq V4 Ultra Low Input kit (Takara) and a NEBNext Ultra DNA Library Prep kit (New England Biolabs), respectively, and sequenced on the Illumina NextSeq (Illumina) by the VIB Nucleomics Core Facility. The preprocessing of the RNA Seq samples was done by Trimmomatic. The adapters were cut off and reads were trimmed when the quality dropped below 20. Reads with a length lower than 35 were discarded. All samples passed quality control based on the results of FastQC. Reads were mapped to the mouse reference genome (mm10) via Tophat2 and counted via HTSeqCount. Samples were subsequently analyzed using R/Bioconductor and the limma procedure was used to normalize and analyze the data. The PCA plot was created using the 15% of genes with the most variable expression. Heatmaps were normalized per mean expression of each gene in all samples. Regulatory networks were selected by Ingenuity Pathway Analysis (IPA) software. We used the online MSigDB webtool (https://www.gsea-msigdb.org/gsea/msigdb) to compute the overlap between our differentially expressed genes and the MSigDB Hallmark gene set. The Hallmark gene set was chosen as they are coherently expressed signatures derived by aggregating many MSigDB gene sets to represent well-defined biological states or processes.

QUANTIFICATION AND STATISTICAL ANALYSIS

Data are represented as mean ± SEM. Statistical significance between experimental groups was assessed using 2-way ANOVA with a Sidak's multiple comparison test. For the body weight, ipGTT and ITT analysis, the data were analyzed as longitudinal data (repeated-measurements over time) using the residual maximum likelihood (REML) as implemented in Genstat v19. Briefly, a linear mixed model (random terms underlined) of the form response = µ + treatment + time + treatment.time + subject.time was fitted to the longitudinal data. The term subject.time represents the residual error term with dependent errors because the repeated-measurements are taken repeatedly from the same subjects, causing correlations among observations. Times of measurement were set as equally spaced, and the best correlation model was selected based on the Aikake Information Coefficient (AIC). Significance of treatment effects over time (i.e., treatment.time) were assessed by an approximate F-test as implemented in Genstat v19. For the C16-Bodipy and 2-NBDG uptake studies: the experiments were laid out with 4 replicates having 1 to 4 observations per treatment, per cell type, per organ and per metabolite. The factor treatment has four levels referring to the 4 combinations of High Fat Diet (HFD) and Standard Diet (SD), with wild-type and knockout genotypes. Data were analyzed separately per organ and per metabolite. Because of the underlying Poisson distribution of cell count data, a log-linear regression model of the form $g(u) = \mu_0 + replicate_i + celltype_j + treatment_k + celltype_j \times treatment_k + \varepsilon_{ijkl}$, with a log link function g(u) was fitted to the data. T statistics were used to assess the significance of treatment effects (on the log scale) by pairwise comparisons to the reference treatment. Estimated mean and standard error of the mean (sem) values were formed on the scale of the response variable.